

***RXTE* Studies of Long-Term X-ray Spectral Variations in 4U 1820-30**

P. F. Bloser, J. E. Grindlay, P. Kaaret

*Harvard-Smithsonian Center for Astrophysics,
60 Garden Street, Cambridge, MA 02138
pbloser@cfa.harvard.edu*

W. Zhang, A. P. Smale

*Laboratory for High Energy Astrophysics, Goddard Space Flight Center,
Greenbelt, MD 20771
zhang@xancus10.gsfc.nasa.gov*

and

D. Barret

*Centre d'Etude Spatiale des Rayonnements, CNRS/UPS,
9 Avenue du Colonel Roche, 31028 Toulouse Cedex 04, France
Didier.Barret@cesr.fr*

ABSTRACT

We present the results of detailed spectral studies of the ultra-compact low mass X-ray binary (LMXB) 4U 1820-30 carried out with the *Rossi X-ray Timing Explorer* (*RXTE*) during 1996-7. 4U 1820-30 is an “atoll” source X-ray burster (XRB) located in the globular cluster NGC 6624. It is known to have an 11 minute binary period and a ~ 176 day modulation in its 2–12 keV flux. Observations were made with the PCA and HEXTE instruments on *RXTE* at roughly one-month intervals to sample this long-term period and study flux-related spectral changes. We find that the 176-day period corresponds to normal atoll source motion in the color-color diagram, indicating that the long period is due to mass accretion rate changes. There are clear correlations between our fitted spectral parameters and both the broad-band (2–50 keV) flux and the position in the color-color diagram, as described by the parameter S_a introduced by Méndez et al. (1999). The hard X-ray tail becomes more prominent at low flux levels as the source moves into the island state. In addition, we find a strong correlation between the position in the color-color diagram and the frequencies of the kilohertz quasi-periodic oscillations (kHz QPOs) reported by Zhang et al. (1998). This lends further support to the notion that evidence for the last stable orbit in the accretion disk of 4U 1820-30 has been observed. For a model consisting of Comptonization of cool photons by hot electrons plus an additional blackbody component, we report an abrupt change in

the spectral parameters at the same accretion rate at which the kHz QPOs disappear, suggesting a change in the accretion flow that affects both the spectrum and the timing properties. For a model consisting of a multicolor disk blackbody plus a cut-off power law, we find that the inner disk radius reaches a minimum at the same accretion rate at which the kHz QPO frequency saturates, as expected if the disk reaches the last stable orbit. Both models face theoretical and observational problems when interpreted physically for this system.

Subject headings: accretion, accretion disks — stars: individual (4U 1820-30) — stars:neutron — X-rays:stars

1. Introduction

The broad-band spectral sensitivities of two X-ray astronomy spacecraft, the *Rossi X-ray Timing Explorer* (*RXTE*, Bradt, Rothschild, & Swank 1993) and *BeppoSAX* (Boella et al. 1997), combined with the high timing resolution of *RXTE*, have allowed major advances in recent years in the study of Low Mass X-ray Binaries (LMXBs). Progress has been particularly rapid in the field of X-ray bursters (XRBs), binary systems containing a low-magnetic field neutron star (NS) accreting matter from a late-type companion star via Roche lobe overflow. It had become apparent by the mid 1990’s that NS systems were capable of producing hard X-ray ($\gtrsim 20$ keV) emission, as indicated by BATSE and SIGMA detections of several XRB at ~ 100 keV (Barret & Vedrenne 1994, Tavani & Barret 1997 and references therein). This eliminated hard X-ray radiation as a unique identifier of black hole (BH) systems, but the limited sensitivity and spectral resolution of these instruments, together with the lack of simultaneous soft X-ray observations, did not allow the spectral shape to be studied in detail or possible differences between NS and BH hard X-ray properties to be determined. The two new satellites are revolutionary due to their broad spectral coverage: the Proportional Counter Array (PCA) and High Energy X-ray Timing Experiment (HEXTE) instruments on *RXTE* cover the range 2–150 keV, while the suite of narrow-field instruments (NFIs) on *BeppoSAX* combine to cover 0.1–200 keV. Many XRB have now been observed with these experiments, allowing detailed modeling of the complete X-ray to hard X-ray spectra with a variety of complex models (e.g., Church et al. 1998; Guainazzi et al. 1998; in ’t Zand et al. 1999; Olive et al. 1999, Piraino et al. 1999a; Piraino et al. 1999b; Barret et al. 1999, 2000).

In addition to broad spectral coverage, *RXTE* offers unprecedented timing resolution ($\sim 1\mu\text{s}$) due to the large collecting area of the PCA. This has led directly to the discovery of quasi-periodic oscillations (QPOs) with frequencies near 1000 Hz (kHz QPOs) in the X-ray timing power spectra of many NS systems (Strohmayer et al. 1996; van der Klis et al. 1996). Since kilohertz frequencies are naturally associated with orbital timescales near a NS, it is generally accepted that the kHz QPOs are produced in the inner accretion disk and that the frequency is related to the inner disk radius. If this is true, the kHz QPOs are a potentially valuable probe of strong field gravity

(Kaaret & Ford 1997). In particular, the relationship between QPO frequency and accretion rate should provide a means to test for the existence of the marginally stable orbit predicted by general relativity (Kaaret, Ford, & Chen 1997; Zhang, Strohmayer, & Swank 1997).

In this paper we present the results of *RXTE* observations of 4U 1820-30, an XRB with a particularly colorful history. 4U 1820-30 is located in the core of the globular cluster NGC 6624 and was one of the first globular cluster X-ray sources discovered (Giacconi et al. 1974). The distance to NGC 6624, 6.4 ± 0.6 kpc, was derived by Vacca et al. (1986) from a study of horizontal branch stars. Thus the distance to 4U 1820-30 is among the better known of all X-ray sources. It is the brightest globular cluster source, and was the first identified X-ray burster (Grindlay et al. 1976). The source has been observed to shift between a high and a low state with a period of about 176 days (Priedhorsky & Terrell 1984); in the All Sky Monitor (ASM) on *RXTE* the 2–12 keV flux varies by typically a factor of ~ 3 and as much as a factor of ~ 6 between the two states (see Figure 1). Also observed is an 11 minute (685 s) period believed to be the orbital period, the shortest known orbital period of all cosmic binary systems (Stella, Priedhorsky, & White 1987). Such a short period suggests that the mass-donating star is a helium dwarf with a mass of 0.06–0.08 M_{\odot} (Rappaport et al. 1987). Two simultaneous kHz QPOs were detected in the persistent flux from 4U 1820-30 by Smale, Zhang, & White (1997).

The goal of the present investigation is to observe the broad-band (2–150 keV) spectrum of 4U 1820-30 with the PCA and HEXTE instruments on *RXTE* and to study the relationships between spectral parameters, kHz QPO frequencies, and accretion rate. The steady 176-day variation of the flux from 4U 1820-30 is most likely due to modulation of the accretion flow, since X-ray bursts are only observed in the low state (Stella, Priedhorsky, & White 1987), and so this source provides a good laboratory for the study of accretion-related spectral changes. We have observed 4U 1820-30 over the course of a year at roughly monthly intervals to sample the entire 176-day period. This same data set was used to study timing properties by Zhang et al. (1998). In Section 2 we describe previous spectral and timing observations of 4U 1820-30. In Section 3 we describe the observations and our analysis procedure. The results are presented in Section 4, discussed in Section 5, and we state our conclusions in Section 6.

2. Previous Observations of 4U 1820-30

As evidenced by its long history, 4U 1820-30 is an extremely well-studied system. In this section we briefly review previous spectral and timing observations of the source.

2.1. Spectral Observations

4U 1820-30 has previously been observed by *ANS*, *EXOSAT*, *Ginga*, *ASCA*, *Einstein*, and *Bep-poSAX*. A wide variety of models have been used to fit the recorded spectra, but the most successful

have been two-component models consisting of either optically thin thermal bremsstrahlung plus a blackbody (TB + BB), a power law with exponential cutoff (an analytical approximation of unsaturated Comptonization) plus a blackbody (CPL + BB), or a more detailed Comptonization model developed by Sunyaev & Titarchuk (1980) plus a blackbody (CompST + BB, after the *CompST* model in XSPEC). Models based on optically thin thermal bremsstrahlung are widely believed to be unphysical for XRB, since the emission measures typically derived ($\sim 10^{60} \text{ cm}^{-3}$) imply, for small optical depths, that the plasma cloud has a radius $\sim 10^{10} \text{ cm}$, too large to be heated to several keV by the neutron star (White et al. 1986; Christian & Swank 1997). We therefore restrict our attention to the CPL and CompST (with or without a BB) model results. The important parameters for the CPL + BB model are the blackbody temperature kT_{BB} , the power law photon index α , and the exponential cutoff energy E_c . For the CompST + BB model, the parameters of interest are kT_{BB} and the temperature kT_e and optical depth τ of the Comptonizing electron cloud, assumed here to be spherical. Photoelectric absorption at low energies by the interstellar medium must be included as well, given by the equivalent hydrogen column density N_H (found using the absorption cross sections of Morrison & McCammon(1983)). Finally, a gaussian line feature at $\sim 6.7 \text{ keV}$ is often required, representing a blend of $K\alpha$ emission lines from helium-like ions of iron (Fe XXV or XXVI; White et al. 1986; Hirano et al. 1987). A summary of previously-reported spectral fits using these models is given in Table 1 and shown graphically in Figure 10; we discuss them briefly here.

Intensity-related spectral changes were first reported for 4U 1820-30 by Parsignault & Grindlay (1978) using *ANS*/HXX data and a power law fit. They found that the photon index α varied between ~ 2 at high count rates and ~ 1.4 at low count rates, indicative of spectral hardening at low luminosity. More complex models could be used after the *EXOSAT* ME instrument observed 4U 1820-30 between 1984 and 1985 (Stella, White, & Priedhorsky 1987), finding a high state luminosity (1–30 keV) of $6.0 \times 10^{37} \text{ ergs s}^{-1}$ and a low state luminosity of $2.0 \times 10^{37} \text{ ergs s}^{-1}$. Fits with the CPL + BB model (Stella, White, & Priedhorsky 1987) gave low state values of $\alpha = 2.5$, $E_c > 30 \text{ keV}$, and $kT_{BB} = 2.3 \text{ keV}$, while in the high state α decreased to 1.7, E_c decreased to $\sim 12 \text{ keV}$, and kT_{BB} fell to 2.0 keV. Note that the inclusion of an exponential cutoff has changed the intensity-related behavior of α compared to the *ANS* results; the softening of the spectrum is now described by the lower cutoff energy while α describes the spectrum below this. White, Stella, & Parmar (1988) fitted the CompST + BB model to the *EXOSAT* data and found that between the low and high states kT_{BB} decreased from 2.06 to 1.61 keV, kT_e fell slightly from 3.5 to 3.3 keV, and τ decreased from 13.2 to 11.9. For both models the ratio of blackbody to “hard component” flux L_{BB}/L_H decreased from 50% to 25% as the luminosity increased. In a similar energy band, the *Ginga* LACs observed 4U 1820-30 at two different intensity levels in 1987 May (Ercan et al. 1993), but the power law was steeper with a lower cutoff than in the *EXOSAT* spectrum (Table 1). The ratio L_{BB}/L_H was similar however.

Lower energy coverage was provided by *ASCA*/GIS and *Einstein* observations. *ASCA* observed 4U 1820-30 in 1993 in the low state and the spectrum (0.6–11 keV) was fitted with the CompST +

BB model (Smale et al. 1994). CompST parameters were similar to those found by *EXOSAT*, but the blackbody temperature was substantially lower ($kT_{BB} = 0.76 \pm 0.02$ keV). Christian & Swank (1997) report on an *Einstein* (SSS + MPC) observation (0.5–20 keV) of 4U 1820-30 from 1978. The luminosity was 5.5×10^{37} ergs s⁻¹, indicative of the high state, and yet fitting the CompST + BB model gave parameters very similar to those from *ASCA* (Table 1). The blackbody flux was only 6% of the CompST flux.

The first observations of 4U 1820-30 extending above ~ 30 keV were made by the NFIs (0.1–200 keV) on *BeppoSAX* in 1998 (Piraino et al. 1999a; Kaaret et al. 1999). These were the first truly broad-band observations, though they covered only a narrow range in luminosity (Table 1). A CPL + BB fit to the 0.3–40 keV spectrum gave $kT_{BB} = 0.47$ keV, $\alpha = 0.55$, and $E_c = 4.5$ keV, while the CompST + BB model yielded $kT_{BB} = 0.46$ – 0.66 keV, $kT_e = 2.83$ keV, and $\tau = 13.7$. Thus the instruments with response below 1 keV consistently find low values of kT_{BB} . The entire range of luminosities observed so far with all instruments has yielded very similar values for the parameters of the CompST + BB model.

The *BeppoSAX* Phoswich Detection System (PDS) failed to detect 4U 1820-30 above 40 keV, consistent with the failure of BATSE to detect the source (20–100 keV) over the first four years of the *CGRO* mission (Bloser et al. 1996). Thus 4U 1820-30 is not a member of the class of XRB detected at ~ 100 keV.

2.2. KiloHertz QPOs

Two simultaneous kHz QPOs were discovered in the persistent emission of 4U 1820-30 by Smale, Zhang, & White (1997) using *RXTE*/PCA data from 1996 October. The characteristics of the QPOs were similar to those found in other XRB: their centroid frequencies were correlated with the 2–60 keV PCA count rate, but the frequency difference remained constant at 275 ± 8 Hz. The fractional rms amplitudes increased dramatically with energy. Zhang et al. (1998) studied monthly PCA observations of 4U 1820-30 (the same data set reported on here; see Section 3) and found that the frequencies of the QPOs are only correlated with PCA count rate below a critical value. Above this, the QPO frequencies remain constant while the count rate increases. Saturation of QPO frequency at high mass accretion rates is an expected signature of the marginally stable orbit (Miller, Lamb, & Psaltis 1998; Kaaret, Ford, & Chen 1997); however, Méndez et al. (1999) have shown that PCA count rate is not a good indicator of accretion rate. Kaaret et al. (1999) used more reliable estimators of mass accretion rate, broad-band flux and hard color, to show that the frequency saturation is robust and thus strong evidence that the inner disk in 4U 1820-30 does reach the marginally stable orbit at high accretion rates.

3. Observations and Analysis

3.1. *RXTE* Observations and Data Reduction

The PCA instrument on *RXTE* is made up of five Xenon proportional counter units (PCUs, numbered 0–4) sensitive from 2–60 keV with a total area of about 6500 cm² (Bradt, Rothschild, & Swank 1993). The HEXTE instrument consists of two clusters of four NaI(Tl)/CsI(Na) phoswich scintillation detectors sensitive from 15–200 keV with an effective area of 1600 cm²; these clusters rock on and off source to obtain background measurements (Rothschild et al. 1998). The ASM is comprised of three Scanning Shadow Cameras (SSCs) with one-dimensional slit masks and 6° × 90° fields of view that monitor the fluxes of bright X-ray sources several times a day in the 2–12 keV band (Levine et al. 1996).

Sixteen joint PCA/HEXTE pointed observations of 4U 1820-30 were performed at roughly monthly intervals between 1997 February 9 and 1997 September 10. In addition, seven observations made between 1996 October 26 and 31 were included (Smale et al. 1997). The *RXTE*/ASM 2–12 keV light curve of 4U 1820-30 during this period is shown in Figure 1, with the times of our pointed observations marked. Each point represents the one-day average of the ASM count rate. The 176-day modulation is clearly visible and is well-sampled by the pointed observations. The ASM count rate varies from ~ 5 to ~ 30 counts s⁻¹ during this time, or ~ 67 mCrab to ~ 400 mCrab. Assuming a Crab-like spectrum and $N_H = 0.3 \times 10^{22}$ cm⁻² (see below), these low and high state values correspond to 1–20 keV luminosities of $\sim 1.2 \times 10^{37}$ ergs s⁻¹ and $\sim 7.0 \times 10^{37}$ ergs s⁻¹, respectively, consistent with the range of luminosities observed previously (Table 1). The dates, starting times in seconds of Mission Elapsed Time (MET = seconds since 1994 Jan 1, 0h0m0s UTC), and mean PCA count rates (2–16 keV) for all 23 observations are listed in Table 2.

The data were divided into the same 90 segments (persistent emission only, typical length ~ 3000 seconds) used by Zhang et al. (1998) and reduced using the standard *RXTE* analysis tools contained in FTOOLS 4.2. For our color-color diagram and PCA spectral analysis we used the “Standard 2” data, which provide 128 energy channels between 2 and 100 keV with 16-second time resolution. Spectra were extracted with *saextract* v4.0b. Backgrounds were estimated with *pcabackest* v2.1b (October 1998), and the v2.2.1 response matrices (January 1998) were used. For the HEXTE spectral analysis we used event mode (E_8us_256_DX1F) data with the 1997 March response matrices. Event mode data were used instead of the standard archive mode data because the 1996 archive data files were corrupted; this problem has been corrected in the reprocessed distribution of 1996 data. Spectra were extracted with *saextract* and rebinned by a factor of two using *grppha* to provide the same energy bins as standard archive data below 60 keV. Deadtime corrections were computed using *hxtdead* v0.0.1.

3.2. Color-Color Diagram and Parameterization of Accretion Rate

A color-color diagram (CCD) was produced from the PCA data with one point for each of the 90 data segments. Only PCUs 0, 1, and 2 were on continuously during all observations, and so only data from these PCUs are included here. The soft and hard colors are defined as the ratios of background-subtracted PCA count rates in the bands 3.5–6.4 keV and 2.0–3.5 keV, and 9.7–16.0 keV and 6.4–9.7 keV, respectively. The CCD is shown in Figure 2. We observe 4U 1820-30 in all three of the states associated with “atoll” sources (Hasinger & van der Klis 1989): the island state, lower banana branch, and upper banana branch. This confirms that the 176-day modulation is in fact due to variation in the mass accretion rate. Figure 2 shows that we have adequately sampled the long period and observed the source in all of its possible states. Closed symbols indicate data segments in which kHz QPOs were discovered by Zhang et al. (1998), while filled symbols indicate data without kHz QPOs.

It is generally believed that in atoll sources the mass accretion rate \dot{M} increases monotonically as the source moves from the island state, through the lower banana, and into the upper banana branch (Hasinger & van der Klis 1989). Méndez et al. (1999) defined the parameter S_a to measure the position of an atoll source within its CCD and thus parameterize its accretion rate. We follow Méndez et al. (1999) and approximate the shape of the CCD track with a spline, as shown in Figure 2. S_a is then defined as the distance along this curve, as measured from the island state. We arbitrarily set $S_a = 1.0$ at (2.378, 0.650) and $S_a = 2.0$ at (2.671, 0.597) in the CCD. Each data point is assigned the value of S_a of the point closest to it on the curve. The error in S_a is estimated by simply projecting the error bars of the data points onto the curve. Thus we may use S_a in addition to the source luminosity to study accretion rate-related changes in spectral parameters or kHz QPO behavior. The advantage in using S_a instead of the hard color (Kaaret et al. 1999) to track the dependence of QPO frequency on accretion rate is that S_a is more sensitive to changes of state along the nearly horizontal banana branch, which is where the break in QPO frequency observed by Zhang et al. (1998) occurs.

3.3. Spectral Fitting

The spectral analysis was performed using XSPEC v10.0 (Arnaud 1996). Spectra for each PCU and HEXTE cluster were reduced separately and combined within XSPEC. Due to systematic uncertainties in the response matrices, only HEXTE data above 20 keV was used. Several authors have written on systematic effects in the PCA and their effect on spectral fitting (e.g. Sobczak et al. 1999; Barret et al. 2000; Wilms et al. 1999; Tomsick et al. 1999); we performed similar investigations and reached similar conclusions. We extracted spectra for each PCU from archival Crab observations spanning the year of our observations (1996 Oct 27, 1997 Mar 22, 1997 Jul 26, and 1997 Dec 15) and fit them with an absorbed power law. Initially we used response matrices generated by *pcarmf* v3.5, but we got very poor fits with large systematic deviations in the residuals,

especially around 5 keV. The residuals were far better using the v2.2.1 response matrices for all four Crab observations, and so we used these for all our 4U 1820-30 fits. The residuals still showed large systematic effects below 2.5 keV and above 20 keV, and so we restricted our fits to this energy range. We also found, as have other authors, that the residuals in PCUs 2 and 3 are considerably worse than those in PCUs 0, 1, and 4. For this reason we use only PCUs 0, 1, and 4 in our fits. PCU 4 was on during all observations except 1997 May 28. The relative normalizations of the three PCUs and two HEXTE clusters were left as free parameters, since there still exist large uncertainties in the relative flux normalizations. In our Crab fits, all three PCUs find power law normalizations 20%–30% higher than the accepted value of ~ 10 photons $\text{cm}^{-2} \text{s}^{-1} \text{keV}^{-1}$ at 1 keV (e.g. Jung 1989). Tomsick et al. (1999) have reported similar results. All spectral model normalizations reported here are obtained from PCU 0; in Tables 3– 5 (and also Figure 5) we report the flux values found directly by PCU 0, while when comparing luminosities with previous measurements (Figure 10) we reduce the PCA values by 15% (see Section 5). A systematic error of 1% was added to all PCA channels using *grppha*. In Figure 3 we show two representative PCA and HEXTE spectra of 4U 1820-30, one from the low island state and one from the high banana state. The hardening of the spectrum at low luminosity is clear. In the island state the source is detected by HEXTE only up to 50 keV, confirming the lack of a detection above this by *BeppoSAX* (Piraino et al. 1999) and BATSE (Bloser et al. 1996).

For our spectral analysis data segments were grouped according to their position in the CCD as follows: Spectra were extracted for each of the 90 data segments. The four island state segments were combined into one spectrum, and the five uppermost banana state segments were each analyzed as separate spectra. In between, data segments were grouped into 26 bins of width 0.025 in S_a and combined together, with an average value of S_a and the total exposure time computed for each bin. Thus we had a total of 32 spectra to fit (see Tables 3– 5).

All spectra were initially fit with two models: the CPL model described in Section 2, and the recently-developed Comptonization model of Titarchuk (1994), called the *CompTT* model in XSPEC. This model improves on the CompST model by including relativistic effects and extending the theory to work in both the optically thin and thick cases. In addition to the Comptonizing electron temperature kT_e and optical depth τ , an additional parameter is the temperature of the cool seed photons kT_W , assumed to follow a Wien law. We consider only a spherical geometry for comparison with previous results. In nearly all cases the model fits were improved by the addition of a blackbody component. We also included a gaussian line component at ~ 6.7 keV in all spectra and a smeared absorption edge in the island state, as described in more detail in Section 4.2.

Some XRB have recently been fit with a multi-color disk blackbody (DBB; Mitsuda et al. 1984) instead of a simple single-temperature BB to account for the soft excess (Guainazzi et al. 1999; Barret et al. 1999). We also fit all our spectra with a model consisting of a CPL plus this disk blackbody (CPL + DBB model). The DBB model parameters are the color temperature of the inner disk kT_{in} and the projected inner disk radius $R_{in}\sqrt{\cos\theta}$, where θ is the inclination of the system. It is expected, however, that the true spectrum emitted by the accretion disk will be that of

a “diluted blackbody” due to the effects of electron scattering, and the DBB parameters must then be modified by a spectral hardening factor f (Ebisawa et al. 1994). The effective temperature and inner radius are $kT_{eff} = kT_{in}/f$ and $R_{eff} = f^2 R_{in}$. Shimura & Takahara (1995) have found that $f = 1.7$ is a good approximation for accretion parameters appropriate for an XRB. We attempted also to fit a CompTT + DBB model, but the data were unable to constrain kT_e and τ for this combination.

The insensitivity of the PCA below 2 keV did not allow us to determine the hydrogen column density N_H from our spectral fits. It was therefore necessary to freeze N_H at previously-determined values for all spectra. Optical reddening for NGC 6624 has been measured by Liller & Carney (1978) and Peterson (1993) to be $E_{B-V} \sim 0.27$, which, using the canonical relationship $A_V = 3E_{B-V}$, yields an optical extinction $A_V = 0.81$. Predehl & Schmitt (1995) find that $N_H = 1.79 \times 10^{21} A_V \text{ cm}^{-2}$, and this gives a value of $N_H \sim 1.4 \times 10^{21} \text{ cm}^{-2}$ for NGC 6624. Previous X-ray observations of 4U 1820-30 with good low energy coverage (*Einstein*, *BeppoSAX*; Smale et al. (1994) do not report a value from *ASCA*) gave $N_H \sim 2.9 \times 10^{21} \text{ cm}^{-2}$, and *EXOSAT* found $N_H \sim 4 \times 10^{21} \text{ cm}^{-2}$ (see Table 1). Predehl & Schmitt (1995) list values of $2.1\text{--}3.6 \times 10^{21} \text{ cm}^{-2}$ for 4U 1820-30 from *ROSAT* data. These values are all in good agreement, and we therefore took a rough average and set $N_H = 3.0 \times 10^{21} \text{ cm}^{-2}$ and kept it frozen for all our spectral fits.

4. Results

4.1. Saturation of QPO Frequency

The frequencies of the kHz QPOs reported by Zhang et al. (1998) are plotted as a function of S_a , as derived here, in Figure 4. Open and filled plotting symbols indicate the lower and higher frequency QPOs, respectively, as defined by Zhang et al. (1998). There is a clear correlation of QPO frequency with S_a below $S_a \sim 1.3$, and then the frequency saturates even though S_a continues to rise. This is an expected signature of the inner disk reaching the marginally stable orbit (Miller, Lamb, & Psaltis 1998). The QPOs disappear completely at $S_a \sim 1.45$. These two “special” values of S_a are indicated in Figure 2. If S_a , the position of the source in the CCD, may indeed be taken to be an indicator of \dot{M} , then Figure 4 provides strong evidence for the detection of the marginally stable orbit in 4U 1820-30.

We have also investigated the possibility that the shape of the CCD varies with the 685-second orbital period. The CCD was reproduced with bins of 128 seconds, and each point was grouped into one of five phase bins. No significant change in the track described by the CCD was found, as the scatter in the points lay well within the error bars. In addition, we have confirmed that the shape of the frequency- S_a plot in Figure 4 does not become smeared out when smaller time bins (and their associated larger error bars) are used.

4.2. Evolution of Spectral Parameters

The 32 combined PCA/HEXTE spectra were first fit with the CPL + BB model with a gaussian line whose parameters were free to vary. Figure 5 shows the gaussian centroid energy E_l and width (σ) as a function of the total luminosity in the 2–50 keV band spanned by both instruments (see also Table 3). In all but the low island state observation the gaussian parameters are consistent with constant values of $E_l \sim 6.8$ keV and $\sigma \sim 0.8$ keV. These are reasonable values for an Fe XXV or XXVI $K\alpha$ line reflected from the inner regions of a hot disk (White et al. 1986; Hirano et al. 1987). The island state line energy is 6.53 keV, suggestive of reflection from less highly ionized gas, but the difference is only $\sim 2\sigma$ and it is difficult to see how the ionization could change so much for only a $\sim 14\%$ change in luminosity. We therefore froze E_l at 6.8 keV and σ at 0.8 keV for our fits with the CompTT + BB model, since we found that the gaussian parameters were less well defined with this choice of continuum. The gaussian parameters were left free for the CPL + DBB fits, and no difference was found between the island and banana state line energies (Table 5).

Since a broad iron line suggests reflection from a disk, we investigated the presence of other reflection components in our spectra. We first attempted to fit a smeared absorption edge (Ebisawa et al. 1994; *smedge* model in XSPEC) between 7 and 8 keV. Only in the island state spectrum could this component be fit with reasonable values. Although we would expect reflection to increase as the accretion rate and disk area increase, this model requires a power law continuum to fit against, and in all the rest of our observations the cutoff energy is too low, resulting in too “curvy” a spectral shape for reliable fitting of the edge with our data. The edge energies in the island state are $8.90^{+0.42}_{-0.38}$ keV for the CPL + BB model and $7.73^{+1.34}_{-0.36}$ keV for the CompTT + BB model, indicative again of ionized material. The smearing width was frozen at 10 keV. These edges are included in the island state fits shown in Tables 3 and 4. The smeared edge could not be fit with the CPL + DBB model. We attempted next to fit the complete XSPEC reflection model *pe xrav* (Magdziarz & Zdziarski 1995) to the island state spectrum. This model is the combination of a cut-off power law with a Compton reflection component. The derived reflection scaling factor was consistent with zero for $\cos\theta = 0.45$. We conclude that, other than the broad iron line, we have only marginal evidence for reflection from the disk, and only in the low state.

The best-fit spectral parameters for the CPL + BB model are given in Table 3, the parameters for the CompTT + BB model are given in Table 4, and the parameters for the CPL + DBB model are given in Table 5. In all three Tables we give the average value of S_a for the included data, and in Table 3 we list the total integration time for the PCA and HEXTE. The CPL + BB spectral parameters are as in Table 1, with the addition of the effective radius of the BB emitting surface R_{BB} and the equivalent width of the gaussian line. The luminosity and flux ratio L_{BB}/L_H are given for the 2–50 keV band covered by the PCA and HEXTE. (This is the raw luminosity derived directly from the fit.) All of the fits are acceptable, and in many cases the χ^2_ν is so low as to indicate that the systematic errors have been overestimated. In Table 4 we give the best-fit temperature of the seed photons kT_W and the Comptonizing y -parameter, defined as $y = 4kT_e\tau^2/m_e c^2$. We also follow in ’t Zand et al. (1999) and derive the effective Wien radius R_W of the seed photons: the

total flux in the CompTT component is corrected for energy gained by Comptonization by dividing by $1 + y$, and this is set equal to the Wien flux from the surface of a sphere. The expression used is $R_W = 3 \times 10^4 D \sqrt{F_{CompTT}/(1+y)}/(kT_W)^2$ km, where D is the distance in kpc, F_{CompTT} is in $\text{erg cm}^{-2} \text{ s}^{-1}$, and kT_W is in keV. The derived values are listed in Table 4. The quality of the CompTT + BB fits is practically identical to that of the CPL + BB fits; based on the values of χ_ν^2 there is no reason to favor one model over the other. We note however that several of the CompTT + BB fits have very large errors on the BB parameters. In Figure 6 we show two examples of spectra from PCUs 0, 1, and 4 and HEXTE clusters A and B fit with the CompTT + BB model. These are the same two spectra shown in Figure 3; now we show the raw counts with the folded model, the residuals, and the unfolded spectra with each component plotted separately. We note that the “wave” shape seen in the residuals of PCA spectra around 6 keV is still visible. In Table 5 we include the fitted disk parameters kT_{in} and $R_{in}\sqrt{\cos\theta}$ with the standard CPL and gaussian parameters. The fits are again all formally acceptable. We note, however, that in the island state the model is unable to reproduce the measured counts above 40 keV.

In Figure 7 we show the spectral parameters of the CPL + BB and CompTT + BB models as a function of S_a , and thus presumably of \dot{M} . In both models it is clear that the parameters of the hard spectral component are correlated with the accretion rate, especially as the accretion rate become low, in the sense that the spectrum becomes harder as \dot{M} decreases. The cutoff energy E_c in the CPL model and kT_e in the CompTT model both rise as the accretion rate drops. Note that when fitting a CPL model it is not α but E_c that indicates the hardness of the spectrum, since α here is really an indication of the optical depth. This change is not gradual throughout the CCD, however; only as the source moves from the lower banana to the island state do the parameters change appreciably. The optical depth τ of the CompTT model drops at lower \dot{M} , and the power law index α (inversely related to τ in the CPL approximation) rises. This general behavior is consistent with that seen in other sources (e.g., Barret et al. 2000; Christian & Swank 1997).

The most intriguing feature of Figure 7 is that the parameters of the CompTT + BB model show a distinct change at $S_a \sim 1.45$. The ratio L_{BB}/L_H is inversely correlated with S_a below this, but becomes constant above. The blackbody temperature kT_{BB} drops from ~ 2.3 keV to ~ 1.6 keV, and the blackbody radius R_{BB} begins to increase from ~ 1 km to ~ 2 km. The τ versus S_a curve also seems to roll over and become nearly constant at this value of S_a . In fact, τ and L_{BB}/L_H appear strongly anti-correlated below $S_a = 1.45$. No such abrupt change is seen in the parameters L_{BB}/L_H , kT_{BB} , R_{BB} , or α of the CPL + BB model. The cutoff parameters E_c in the CPL model and kT_e in the CompTT model do not seem to change at $S_a = 1.45$; however, both appear to change from strong anti-correlations with S_a to near-constant values at $S_a \sim 1.3$. These “special” values of $S_a = 1.3$ and $S_a = 1.45$ are especially interesting because, as shown in Section 4.1 above, these are the same values at which the kHz QPOs saturate in frequency and disappear completely, respectively. Thus the accretion flow must be changing at the values of \dot{M} corresponding to these values of S_a in a way that affects both the energy spectrum and the frequencies of the kHz QPOs.

The fact that this correlation is seen only with the CompTT + BB model suggests that this model is the more accurate description of the spectrum. In Figure 8 we show the seed photon temperature kT_W and the Wien radius R_W described above as a function of S_a . Although the error bars are large, there is an indication that the temperature and radius are anticorrelated below $S_a = 1.3$ and constant above. This is precisely the behavior expected if the seed photons are coming from the inner part of the accretion disk, and the disk is contracting until it reaches the last stable orbit at $S_a = 1.3$ as indicated by the kHz QPOs. This trend gives us confidence in the fitted values of kT_W , which must still be treated with some caution because the peak of the Wien spectrum at $3kT_W$ lies below the PCA energy range. The large values of the Wien radius also suggest that the seed photons originate in the disk.

The parameters for the CPL + DBB model are shown in Figure 9. The cut-off power law components behave similarly to those in the CPL + BB model, though the values of α and E_c are both considerably lower. This is because the DBB model prefers lower temperatures than the simple BB, and so the curvature in the spectrum at higher energies must now be described by a lower cutoff value. The behavior of the DBB component is of great interest: kT_{in} rises and R_{in} falls with increasing accretion rate until $S_a \sim 1.3$, then both remain nearly constant (though there is some indication that kT_{in} continues to rise slowly). The fraction of the total luminosity in the DBB component increases with S_a in the same manner. Thus it appears that the accretion disk inner radius grows smaller and hotter as the accretion rate increases until the last stable orbit is reached at $S_a = 1.3$. This behavior of the DBB component is consistent with that expected from the behavior of the kHz QPOs. Thus this model is also compelling as an accurate physical description of the system.

5. Discussion

5.1. Comparison with Previous Spectral Measurements

First we compare our spectral results for 4U 1820-30 to those previously reported using the CPL + BB and CompTT + BB models. In Figure 10 we show our *RXTE* spectral parameters together with the previously-reported parameters described in Section 2.1 and Table 1. Here we plot the spectral parameters as a function of the total 2–50 keV luminosity, assuming a distance of 6.4 kpc. The luminosities of the previous measurements have been translated into the 2–50 keV band based on the reported parameters and fluxes. The integrated 2–50 keV flux in the archival Crab spectra (see Section 3.3) is $\sim 15\%$ higher than what is expected; therefore, the *RXTE* luminosities in Figure 10 have been divided by a factor of 1.15 for proper comparison to previous instruments. It is immediately obvious that there is considerable disagreement between different instruments. In general, the *RXTE* spectral parameters agree most closely with those found by *EXOSAT* and *Ginga*, and differ the most from those found by *BeppoSAX*. More specifically, the *RXTE* BB component parameters agree fairly well with those found by *EXOSAT* and *Ginga* for the CPL + BB model

and with those found by *EXOSAT* for the CompTT + BB model. In the CompTT + BB model, for example, *EXOSAT* also observed kT_{BB} to decrease from $\gtrsim 2$ keV to ~ 1.5 keV between the low and high states, while R_{BB} increased from ~ 1.7 km to ~ 3.7 km. The *EXOSAT* CPL parameters also agree well with our values in the low and high states, as do the *Einstein* values (Christian & Swank (1997) do not report BB values for the CPL model with *Einstein*). The *BeppoSAX* BB parameters and CPL spectral index α differ considerably from ours. All of the experiments that used a CompST model found Comptonization parameters that agree well with our CompTT parameters at high luminosity. In the low state, however, *EXOSAT* did not observe the increase in kT_e and decrease in τ that we see. It is strange that the *EXOSAT* low state observation could only place a lower limit of ~ 30 keV on E_c for the CPL model, yet could still constrain such a low $kT_e \sim 3.5$ keV for the CompST model. It is apparent that our island state observation is the first observation of 4U 1820-30 in the low state since *EXOSAT*, and it is puzzling that the Comptonization parameters differ so much. Further observations in the island state are needed, but the low duty cycle in this state seen in Figure 1 makes this difficult.

It is apparent from Table 1 and Figure 10 that those experiments without sensitivity below 1 keV, i.e. *EXOSAT*, *Ginga*, and *RXTE*, find consistently higher kT_{BB} and lower R_{BB} than do those instruments with sensitivity below 1 keV, i.e. *ASCA*, *Einstein*, and *BeppoSAX*. The differences are important to the question of the origin of the soft component of the spectrum. The instruments with low energy sensitivity find $R_{BB} \gtrsim 10$ km, consistent with the radius of a neutron star. The other instruments, including *RXTE*, find $R_{BB} \lesssim 4$ km, implying that the blackbody component can come from only a limited region of the neutron star surface, such as an optically thick boundary layer. (An alternate explanation for apparently small blackbody radii for XRBs given by Rutledge et al. (1999), that a blackbody is not an appropriate model and fits with hydrogen atmosphere models give radii near 10 km, is not applicable to 4U 1820-30 since the accretion rate is too high.) We have attempted to fit our *RXTE* spectra with a BB component with $kT_{BB} < 1$ keV, forcing the fit to find a new local minimum. For a CompTT + BB model of this type, kT_{BB} remained nearly constant at ~ 0.6 keV while R_{BB} stayed at ~ 24 km, too large for a NS surface. The seed photon energy kT_W decreased from 1.8 keV to 1 keV as S_a increased from 1.0 to 1.4, which also seems unphysical, and neither kT_e nor τ changed their behavior at the interesting values of S_a . The new model was unable to reproduce the observed counts at energies above 30–40 keV in the island state. This, together with the clear change in the behavior of our BB parameters at an “interesting” value of S_a (or L) seen in Figure 7, leads us to conclude that the BB component parameters listed in Tables 3 and 4 are the best fits to our data for the CPL + BB and CompTT + BB models. We note, however, that properly measuring low energy components depends on having the correct N_H , which we cannot measure with the PCA, and so it is entirely possible that additional components exist in the true spectrum. This notion is perhaps supported by the fact that the seed photon temperature found in the CompTT + BB model is in good agreement with the BB temperature found by *BeppoSAX*.

5.2. Physical Interpretation of the CompTT + BB and CPL + DBB Models

Our *RXTE* data on 4U 1820-30 may be described equally well by two different physically-motivated models (CompTT + BB and CPL + DBB), both of which have parameters that appear to “know” about the saturation of kHz QPO frequency at the accretion rate corresponding to $S_a = 1.3$. The physical interpretation of these two models leads to two different pictures of the origin of the spectral components in XRBs. Neither picture, however, is completely consistent with theoretical and observational constraints.

The question of the origin of the soft and hard spectral components in XRBs has been addressed by many authors (e.g., White, Stella, & Parmar 1988; Guainazzi et al. 1998; Olive et al. 1999, Barret et al. 1999, 2000). Early work supposed that the accretion disk intersects the NS surface in an optically thick boundary layer which is the source of the blackbody component observed in XRBs. A potentially useful diagnostic is the ratio of flux or luminosity in the BB component to the flux in the hard component (L_{BB}/L_H). Sunyaev & Shakura (1986) showed that, if relativistic effects are taken into account, the luminosity of the boundary layer should be at least equal to that of the disk, and can be more than twice it if the disk extends all the way to the marginally stable orbit. We find $L_{BB}/L_H < 0.5$ at all times for the CompTT + BB and CPL + DBB models, and in the CompTT + BB model at high accretion rates it is as low as 0.1. Many authors (White, Stella, & Parmar 1988; Barret et al. 1999, 2000; Table 1) have found similar results for this and other sources. Guainazzi et al. (1998) and Barret et al. (1999) suggest that this implies the weak BB component is produced by an optically thick accretion disk, while the strong CompTT component originates in an optically *thin* boundary layer through a process such as the gap accretion model of Kluźniak & Wilson (1991). Barret et al. (2000), however, argue that the similarities between NS and BH hard X-ray emission require that both be produced by the same mechanism, which rules out boundary layer processes. In addition, Church et al. (1998) have found that the evolution of spectra during X-ray dips in sources such as 4U 1916-05 are consistent with a compact blackbody emitter being occulted while an extended hard X-ray emitter is only partially covered. From timing of dip ingresses and egresses they estimate a diameter of $\sim 4 \times 10^9$ cm for the hard X-ray emitting region. Thus one possibility is that the BB component is produced in an optically thick boundary layer covering a fraction of the neutron star surface, while the CPL or CompTT component comes from an extended hot corona. Some mechanism must then reduce the luminosity of the boundary layer relative to that of the disk and corona. White, Stella, & Parmar (1988) suggest that the NS may be spinning close to equilibrium with the inner edge of the accretion disk, which would lessen the energy dissipated in the boundary layer, but the NS spin periods measured with *RXTE* (typically ~ 300 Hz) are well below this. Another possibility discussed by Barret et al. (2000) is that an optically thick boundary layer does not exist. Instead, within the standard optically thick accretion disk there exists a hot, optically thin phase of the accretion flow such as the advection-dominated solutions of Narayan & Yi (1995). Such a picture has been applied successfully to BH systems (Esin et al. 1998). Barret et al. (2000) suggest that the boundary between such a hot flow and the NS may well be optically thin and thus neither contribute to the BB component (now

coming entirely from the disk) nor quench the hot advective flow and cause it to collapse to a thick disk (Yi et al. 1996). The NS surface must still be a source of cool reprocessed photons, however, and it is not clear what effect this must have.

We can interpret our CompTT + BB model fits for 4U 1820-30 in terms of the former of these two possibilities, in which the 2.3 keV BB flux comes from an optically thin boundary layer and the CompTT component from an extended corona. We have noted that in Figure 7 the ratio L_{BB}/L_H decreases as the optical depth of the Comptonizing cloud increases, and both become nearly constant at the same accretion rate. In Figure 11 we show L_{BB}/L_H as a function of τ ; the two are obviously strongly anticorrelated. Thus perhaps the BB emission from the boundary layer is simply becoming more obscured as the optical depth of the corona increases, and the boundary layer emission is being redistributed to higher energies by the Comptonizing cloud. At the accretion rate corresponding to the break, the ~ 2.3 keV boundary layer could be completely obscured, and a cooler, ~ 1.7 keV disk component would begin to dominate the BB part of the spectrum. This component is emitted from radii outside the inner hot cloud, leading to the upward trend in R_{BB} observed at the same S_a . In this scenario a multicolor disk blackbody model would be preferable for the higher luminosity spectra, but as noted in Section 3.3 fits of a DBB together with the CompTT model were indeterminate.

Such a scenario ties in with the accretion rate-dependence of the kHz QPO frequencies. The origin of kHz QPOs is often explained by means of a “beat-frequency” model. The magnetospheric beat-frequency model (Lamb 1991), which was developed to explain horizontal branch oscillations (HBOs) in Z sources, has been suggested by Strohmayer et al. (1996) as the source of kHz QPO pairs as well. Miller, Lamb, & Psaltis (1998) point out that it is not clear how the X-ray modulation at the orbital frequency of the disk is produced in this model, and that it cannot explain both the HBOs and the kHz QPOs sometimes seen together in Z sources. Instead, Miller, Lamb, & Psaltis (1998) propose the sonic-point beat-frequency model, in which the disk is truncated by radiation drag from the NS which causes clumps of gas to lose energy and fall rapidly inward on spiral trajectories. This spiral pattern crashes onto the star to create X-ray hot spots which rotate at the frequency of the disk inner edge, generating the high frequency QPO. This flow is optically thin, which permits the radiation to exert its drag on the disk in the first place. At the same time, some gas is channeled by the NS magnetic field onto hot spots which rotate at the spin frequency of the star. These hot spots modulate the radiation drag, and thus the brightness of the first hot spots, at the frequency of the beat between the disk orbital and stellar spin frequencies, producing the second QPO. Miller, Lamb, & Psaltis (1998) point out several predictions of this model as the inner edge of the disk, or “sonic point,” approaches the marginally stable orbit. First, the frequencies of the QPOs should increase together up to a certain accretion rate, then remain constant. This is clearly seen in Figure 4. Second, after the marginally stable orbit is reached, the amplitudes of the QPOs should decrease. This is because, as \dot{M} increases further, the optical depth between the sonic point and the NS surface will increase, lessening the radiation drag which produces the modulation in the first place. Zhang et al. (1998) found that the fractional rms amplitudes of the

QPOs steadily decreased as the count rate increased until they disappeared altogether.

Thus we can envision the following scenario: In the island state the inner edge of the disk lies at a radius greater than $6GM/c^2$, within which the sonic-point model is operating. The boundary layer is optically thick, producing blackbody radiation from a small equatorial region of the NS surface. The NS is surrounded by a hot cloud in the form of an accretion disk corona, since the optically thick boundary layer prevents an advection-dominated solution from existing in this case. The Wien temperature and radius also indicate that the corona is supported by the disk. The electron scattering optical depth of the corona is low, and we may see the boundary layer emission. As \dot{M} increases the inner edge of the disk moves inward and the QPO frequencies increase. The optical depth of the corona increases and, as the boundary layer and disk emission increase, the corona is cooled and kT_e drops. The increased emission from the boundary layer does not make it out to the observer, as it goes into cooling the corona. The derived Wien radius also indicates that the disk inner radius is shrinking. When the inner edge of the disk reaches the marginally stable orbit, the QPO frequencies cease rising. The disk has reached its maximum emitting area for cool photons, and so kT_e does not fall any more. Further increasing the accretion rate causes the optical depth of both the corona and the spiraling gas clumps between the disk edge and the boundary layer to rise, reducing the radiation drag that ultimately generates the QPOs. The QPO amplitude begins to decrease until, at the point when the boundary layer is completely obscured, they disappear altogether. At this point the cooler emission from the disk itself is all that can be seen from the outside, resulting in a lower observed kT_{BB} and higher R_{BB} , as the boundary layer powers the optically thick, nearly thermal-looking Comptonizing cloud. The ratio of BB to CompTT flux is quite small at this point.

The main problem with this picture is that the Comptonizing corona is supported by the accretion disk, as indicated by the Wien parameters (Figure 8), and yet its luminosity is always more than twice that of the BB component. If the boundary layer is being obscured by the corona, transferring energy from the soft to the hard component, then the seed temperature of the CompTT model should start to reflect this. Thus if the corona is supported by the disk this picture is not consistent with theoretical constraints on the ratio of the flux from the boundary layer and disk (Sunyaev & Shakura 1986).

Our CPL + DBB model for 4U 1820-30 may be interpreted in terms of a hot advective flow lying within the standard thin accretion disk if the boundary layer between this hot, optically thin flow and the NS may also be optically thin (Barret et al. 2000). The scenario is fairly straight forward in this case. In the island state, the inner disk radius is large and the temperature is low. Between the disk and the NS the hot advective flow Comptonizes soft photons from the disk and NS surface, producing the CPL component. As the disk lies outside the hot corona, it is clearly visible. As \dot{M} increases, the inner disk moves inward and its temperature increases, as shown in Figure 9. As the disk area increases, the ratio of DBB to CPL flux increases, as does the cooling of the hot flow, causing the cutoff energy to drop. The power law index falls as well, indicating an increase in τ . The QPOs may be produced by the same sonic point model as before, and so their

frequency increases. When the inner disk reaches the last stable orbit, the flux ratio, temperature, radius, optical depth, and cutoff energy reach constant values. As \dot{M} continues to rise, kT_{BB} does appear to continue rising slowly as well.

We may use the DBB parameters at the last stable orbit to estimate the mass of the NS, as described by Ebisawa et al. (1994) and Shimura & Takahara (1995). As discussed in Section 3.3, R_{in} must be corrected by a spectral hardening factor; this effective radius is then set to the radius at which the disk temperature becomes a maximum, $5/3$ the inner disk radius itself. Then $3R_S = (3/5) \times 0.6 \times R_{in} f^2$, where R_S is the Schwarzschild radius. The factor of 0.6 accounts for the decrease in $R_{in} \sqrt{\cos \theta}$ due to relativistic effects. Using $f = 1.7$ from Shimura & Takahara (1995) and $R_{in} = 8$ km from Figure 9 gives a NS mass of $M_{NS} = 0.94/\sqrt{\cos \theta} M_\odot$. The NS mass may also be estimated by setting the maximum kHz QPO frequency of ~ 1050 Hz equal to the Keplerian frequency at the last stable orbit. This gives $M_{NS} = 2.1 M_\odot$ for a non-rotating NS. For a NS spin frequency of 275 Hz (Zhang et al. 1998) the relativistic corrections are small. Equating these two masses requires $\theta = 78^\circ$, which is nearly problematic due to the lack of dips from this source. Should any DBB flux be lost due to scattering in the hot corona, however, the true value of R_{in} and thus M_{NS} would appear reduced.

Appealing as this physical model is, it is inconsistent with the observational work of Church et al. (1998), who find that X-ray dips in XRBs may be modeled by partial absorption of a large corona responsible for the hard X-ray emission. They estimate a diameter of 4×10^9 cm for this corona, considerably larger than the $16f^2 = 46$ km = 4.6×10^6 cm allowed from Figure 9 if the hot advective flow is to lie inside the accretion disk. Tomsick, Lapshov, & Kaaret (1998) analyze a dip observed from the BH candidate 4U 1630-47 and find that the power law component of the spectrum is more highly absorbed, in contrast to the situation found by Church et al. (1998) for XRBs. Thus a hot advective Comptonizing flow lying within the accretion disk may be a good model for BH systems, but seems to present a geometry problem for XRBs.

5.3. Lack of Extensive Hard X-ray Emission: NS vs BH Systems

As noted in Section 2.1, 4U 1820-30 does not belong to the class of XRBs detected at ~ 100 keV. Our *RXTE* observations confirm this, as the source is not detected above 50 keV even in the hardest state. Extrapolating the island state spectrum from Table 4 into the BATSE energy range (20–100 keV) gives a hard X-ray luminosity of $\sim 2.5 \times 10^{36}$ ergs s^{-1} , consistent with the upper limit of $\sim 2.8 \times 10^{36}$ ergs s^{-1} found by BATSE (Bloser et al. 1996). The predicted flux at 100 keV in the island state is $\sim 2 \times 10^{-7}$ photons $cm^{-2} s^{-1} keV^{-1}$. From Figure 1 it is clear that the source spends only a small fraction of its duty cycle in the island state, making hard X-ray detection even less likely. Barret, McClintock, & Grindlay (1996; see also Barret et al. 2000) have proposed that XRBs can only produce substantial hard X-ray emission when their soft X-ray (1–20 keV) luminosity is below a critical value of $\sim 1.5 \times 10^{37}$ ergs s^{-1} , and that this may be used to distinguish NS systems from BH systems. Since the 1–20 keV luminosity of 4U 1820-30 never falls

below $\sim 2 \times 10^{37}$ ergs s^{-1} , even in the island state, our lack of detection of the source above 50 keV is consistent with this picture.

6. Conclusions

We have studied the X-ray spectrum of 4U 1820-30 in all three states displayed by atoll sources, including the first observation in the island state since the *EXOSAT* observation described by Stella, White, & Friedhorsky (1987). The fact that the 176-day flux variation corresponds to normal motion in the CCD indicates that the long period is indeed due to modulation in the accretion rate. The spectra are well fit by the CPL + BB, CompTT + BB, and CPL + DBB models, but the parameters of the CompTT + BB and CPL + DBB models show more robust correlations with each other and with the frequencies of the kHz QPOs when plotted as a function of accretion rate (as parameterized by S_a). In the CompTT + BB case, the relative contribution of the blackbody component decreases as the optical depth of the Comptonizing cloud increases until both reach constant values at the same \dot{M} at which the QPOs disappear. This can be understood in terms of simple geometrical arguments and the sonic-point beat-frequency QPO model of Miller, Lamb, & Psaltis (1999) if the blackbody component emanates from an optically thick boundary layer and the hard Comptonized component from an extended cloud; however, the relative fluxes of the two components violate theoretical constraints. In the CPL + DBB case, the behavior of the parameters for the inner accretion disk agree with expectations from the QPOs, but the Comptonizing corona must take the form of a hot advective flow within the standard thin disk; observations of dipping XRBs suggest the corona is much larger than this. The questions raised by both models are central to the issue of hard X-ray production in NS systems. In either case, the saturation of QPO frequency at $S_a = 1.45$ provides strong additional evidence for the detection of the marginally stable orbit in the accretion disk of 4U 1820-30.

We would like to thank Dimitrios Psaltis for early discussions of the data. This paper had made use of quick-look results provided by the ASM/*RXTE* team. This work was supported in part by NASA grant NAG5-7393. PFB acknowledges support from NASA GSRP grant NGT5-50020.

REFERENCES

- Arnaud, K. A. 1996, in ASP Conf. Ser. 101, *Astronomical Data Analysis Software and Systems V*, ed. J. H. Jacoby & J. Barnes (San Francisco: ASP), 17
- Barret, D., Grindlay, J. E., Harrus, I. M., & Olive, J. F. 1999, *A&A*, 341, 789
- Barret, D., McClintock, J. E., & Grindlay, J. E. 1996, *ApJ*, 473, 963
- Barret, D., Olive, J. F., Boirin, L., Done, C., Skinner, G. K., & Grindlay, J. E. 2000, *ApJ*, 533, 329
- Barret, D. & Vedrenne, G. 1994, *ApJS*, 92, 505

- Bloser, P. F., et al. 1996, *A&AS*, 120, 275
- Boella, G., Butler, R. C., Perola, G. C., et al. 1997, *A&AS* 122, 299
- Bradt, H. V., Rothschild, R. E., & Swank, J. H. 1993, *A&AS*, 97, 355
- Christian, D. J., & Swank, J. H. 1997, *ApJS*, 109, 177
- Church, M. J., Parmar, A. N., Balucinska-Church, M., Oosterbroek, T., Dal Fiume, D., & Orlandini, M. 1998, *A&A*, 338, 556
- Ebisawa, K., et al. 1994, *PASJ*, 46, 375
- Ercan, E. N., Cruise, A. M., Kellet, B. J., & Saygili, K. 1993, *MNRAS*, 262, 511
- Esin, A. A., Narayan, R., Cui, W., Grove, J. E., Zhang, S. N. 1998, *ApJ*, 505, 854
- Giacconi, R., Murray, S., Gursky, H., Kellogg, E., Schreier, E., Matilsky, T., Koch, D., Tananbaum, H. 1974, *ApJS*, 27, 37
- Grindlay, J. E., Gursky, H., Schnopper, H., Parsignault, D. R., Heise, J., Brinkman, A. C., & Schrijver, J. 1976, *ApJ*, 205, L127
- Guainazzi, M., Parmar, A. N., Segreto, A., Stella, L., Dal Fiume, D., & Oosterbroek, T. 1998, *A&A*, 339, 802
- Hasinger, G., & van der Klis, M. 1989, *A&A*, 225, 79
- Hirano, T., Hayakawa, S., Nagase, F., Masai, K., & Mitsuda, K. 1987, *PASJ*, 39, 619
- In 't Zand, J. J. M., et al. 1999, 345, 100
- Jung, G. V. 1989, *ApJ*, 338, 972
- Kaaret, P., & Ford, E. C. 1997, *Science*, 276, 1386
- Kaaret, P., Ford, E. C., & Chen, K. 1997, *ApJ*, 480, L27
- Kaaret, P., Piraino, S., Bloser, P. F., Ford, E. C., Grindlay, J. E., Santangelo, A., Smale, A. P., & Zhang, W. 1999, *ApJ*, 520, L37
- Kluźniak, W., & Wilson, J. R. 1991, *ApJ*, 372, L87
- Lamb, F. K. 1991, in *Neutron Stars: Theory and Observation*, eds. J. Ventura & D. Pines (Dordrecht: Kluwer), 445
- Levine, A. M., Bradt, H., Cui, W., Jernigan, J. G., Morgan, E. H., Remillard, R., Shirey, R. E., & Smith, D. A. 1996, *ApJ*, 469, 33
- Liller, M. H., & Carney, B. W. 1978, *ApJ*, 224, 383
- Magdziarz, P., & Zdziarski, A. A. 1995, *MNRAS*, 273, 837
- Méndez, M., van der Klis, M., Ford, E. C., Wijnands, R., & van Paradijs, J. 1999, *ApJ*, 511, L49
- Miller, M. C., Lamb, F. K., & Psaltis, D. 1998, *ApJ*, 508, 791
- Mitsuda, K., Inoue, H., Koyama, K, et al. 1984, *PASJ*, 36, 741

- Morrison, R., & McCammon, D. 1983, *ApJ*, 270, 119
- Narayan, R., & Yi, I. 1995, *ApJ*, 452, 710
- Olive, J. F., Barret, D., Boirin, L., & Grindlay, J. E. 1999, *Adv. Space Res.*, in press
- Parsignault, D. R., & Grindlay, J. E. 1978, *ApJ*, 225, 970
- Peterson, C. 1993, in eds. S. Djorgivski & G. Meylan, *ASP Conf. Series* 50, 337
- Piraino, S., Santangelo, A., Ford, E. C., & Kaaret, P. 1999a, to appear in *Proc. 19th Texas Symp. in Paris*
- Piraino, S., Santangelo, A., Ford, E. C., & Kaaret, P. 1999b, *A&A*, 349, L77
- Predehl, P., & Schmitt, J. H. M. M. 1995, *A&A*, 293, 889
- Priedhorsky, W., & Terrell, J. 1984, *ApJ*, 284, L17
- Rappaport, S., Ma, C., Joss, P. C., & Nelson, L. A. 1987, *ApJ*, 322, 842
- Rothschild, R. E., et al. 1998, *ApJ*, 496, 538
- Rutledge, R. E., Bildsten, L., Brown, E. F., Pavlov, G. C., & Zavlin, V. E. 1999, *ApJ*, 514, 945
- Shimura, T., & Takahara, F. 1995, *ApJ*, 445, 780
- Smale, A. P., Dotani, T., Mitsuda, K., & Zylstra, G. 1994, *BAAS*, 26, 872
- Smale, A. P., Zhang, W., & White, N. E. 1997, *ApJ*, 483, L119
- Sobczak, G. J., McClintock, J. E., Remillard, R., Bailyn, C. D., & Orosz, J. A. 1999, *ApJ*, 520, 776
- Stella, L., Priedhorsky, W., & White, N. E. 1987, *ApJ*, 312, L17
- Stella, L., White, N. E., & Priedhorsky, W. 1987, *ApJ*, 315, L49
- Strohmayer, T. E., Zhang, W., Swank, J. H., Smale, A. P., & Titarchuk, L. 1996, *ApJ*, 469, L9
- Sunyaev, R. A., & Shakura, N. I. 1986, *Sov. Ast. Lett.*, 12, 117
- Sunyaev, R. A., & Titarchuk, L. G. 1980, *A&A*, 86, 121
- Tavani, M. & Barret, D. 1997, in eds. C. Dermer, M. Strickman, & J. Kurfess, *Proc. of the 4th Compton Symp.*, *AIP Conf. Proc.* 410, 75
- Titarchuk, L. 1994, *ApJ*, 434, 570
- Tomsick, J. A., Kaaret, P., Kroeger, R. A., & Remillard, R. A. 1999, *ApJ*, 512, 892
- Tomsick, J. A., Lapshov, I., & Kaaret, P. 1998, *ApJ*, 494, 747
- Vacca, W. D., Lewin, W. H., & van Paradijs, J. 1986, *MNRAS*, 220, 339
- van der Klis, M., et al. 1996, *ApJ*, 469, L1
- White, N. E., Peacock, A., Hasinger, G., Mason, K. O., Manzo, G., Taylor, B. G., & Branduardi-Raymont, G. 1986, *MNRAS*, 218, 129
- White, N. E., Stella, L., & Parmar, A. N. 1988, *ApJ*, 324, 363

- Wilms, J., Nowak, M. A., Dove, J. B., Fender, R. P., & di Matteo, T. 1999, *ApJ*, 522, 460
- Yi, I., Narayan, R., Barret, D., & McClintock, J. E. 1996, *A&AS*, 120, 187
- Zhang, W., Smale, A. P., Strohmayer, T. E., & Swank, J. H. 1998, *ApJ*, 500, L171
- Zhang, W., Strohmayer, T. E., & Swank, J. H. 1997, *ApJ*, 482, L167

Fig. 1.— *RXTE*/ASM light curve of 4U 1820-30 (2–12 keV) from 1996 October – 1997 October (MJD 50400 = 1996 November 12). Each point represents a 1-day average. Pointed PCA/HEXTE observation times are marked with vertical lines. The ~ 176 day modulation is clear.

Fig. 2.— Color-color diagram of 4U 1820-30. Each point represents one of the 90 data segments from Zhang et al. (1998), which have typical lengths of 3000 s. The soft and hard colors are defined as the ratio of background-subtracted count rates in the bands 3.5–6.4 keV and 2.0–3.5 keV, and 9.7–16.0 keV and 6.4–9.7 keV, respectively. Filled symbols indicate data that contain kHz QPOs from Zhang et al. (1998), open symbols data that do not. The position within the diagram is parameterized by the variable S_a , the distance along the fitted line. Important values of S_a are indicated in the Figure for clarity.

Fig. 3.— Representative PCA (PCU 0) and HEXTE (cluster A) spectra of 4U 1820-30. On 1997 July 16 the source was in a high state, in the upper banana portion of the color-color diagram. On 1997 May 2 the source was in the low island state and is detected with HEXTE up to 50 keV. The hardening of the spectrum with decreasing luminosity is clear.

Fig. 4.— Relation between kHz QPO frequency and position within the color-color diagram, measured by the parameter S_a . Filled and open symbols represent the high and low frequency QPOs, respectively. There is a clear saturation in QPO frequency even though S_a , and thus presumably the accretion rate, continues to rise.

Fig. 5.— Fitted centroid energy and width (σ) of the gaussian line as a function of total luminosity (2–50 keV) for the CPL + BB model. With the exception of the island state observation, the centroid energy remains constant at ~ 6.8 keV and the width remains constant at $\sigma \sim 0.8$ keV, indicative of reflection from ionized gas in the disk. The line energy in the island state, ~ 6.55 keV, suggests less ionized gas, but the difference is only $\sim 2\sigma$. A smeared absorption edge at 8.9 keV is included in the island state fit.

Fig. 6.— Examples of 4U 1820-30 spectra fit with the CompTT + BB model. The top panel shows the raw count rate spectrum with the fitted model folded through the instruments’ responses, the middle panel shows the residuals of the fit, and the bottom panel shows the unfolded spectrum with the individual model components. The dotted line is the blackbody, the dashed line is the CompTT model, and the dash-dot line is the gaussian line. On the left is the island state spectrum of 1997 May 2, and on the right is the banana state spectrum of 1997 July 16 (first segment); see Table 4 for the fitted parameters.

Fig. 7.— Variation of spectral parameters for CPL + BB and CompTT + BB models with accretion rate, parameterized by S_a . Here kT_{BB} = blackbody temperature, R_{BB} = blackbody radius, α = power law photon index, and E_c = power law cut-off energy, τ = Comptonization optical depth and kT_e = Comptonizing electron temperature. Error bars are 1σ for one interesting parameter.

Fig. 8.— The temperature of the seed photon distribution kT_W from the CompTT + BB model,

with the effective Wien radius R_W described in the text. The temperature and radius are anticorrelated below $S_a \sim 1.3$ and constant above.

Fig. 9.— Variation of CPL + DBB parameters with S_a . Here kT_{in} = temperature of inner disk and $R_{in}(\cos \theta)^{1/2}$ = inner disk radius with inclination θ , while α and E_c are as in Figure 7. Error bars are 1σ for one interesting parameter.

Fig. 10.— Comparison of *RXTE* spectral parameters with previous measurements (see Table 1) as a function of total 2–50 keV luminosity. The luminosities of the previous measurements have been translated into the 2–50 keV band based on the reported parameters and fluxes. *EXOSAT* = open circle; *Ginga* = square; *ASCA* = diamond; *Einstein* = cross; *BeppoSAX* = hourglass. The luminosities of the *RXTE* fits have been divided by a factor of 1.15 based on fits to the Crab (see text).

Fig. 11.— The ratio of blackbody luminosity to CompTT luminosity L_{BB}/L_H as a function of τ in the CompTT + BB model. The two are strongly anticorrelated; as the optical depth of the Comptonizing cloud increases, the relative contribution of the blackbody decreases.

Table 1. Previously-Reported Spectral Fits of 4U 1820-30^a

Date(s)	N_H^b (10^{22} cm^{-2})	kT_{BB}^c (keV)	α^d	E_c^e	kT_e^f (keV)	τ^g (keV)	E_l^h (keV)	L
<i>ANS HXX</i> (1–28 keV)								
1975 Mar 24-8	1.3 ± 0.3	...	2.12 ± 0.08	~ 6.7	14
1975 Sep 26-30	< 1.0	...	1.41 ± 0.30	~ 6.7	3
1976 Mar 23-7	0.93 ± 0.3	...	1.89 ± 0.08	~ 6.7	14
<i>EXOSAT ME</i> (1–30 keV)								
1984 Sep 26	0.4 ± 0.1	2.0	1.7	12.0	6
1985 Apr 16								
1985 Sep 22-3	0.39	1.61	3.3	11.9	6.7	5
1985 Aug 19-20	0.4 ± 0.1	2.3	2.5	> 30	2
	0.52	2.06	3.5	13.2	6.7	2
<i>Ginga LAC</i> (1–20 keV)								
1987 May 1-2	0.95 ± 0.22	2.35 ± 0.12	2.21 ± 0.14	4.71 ± 0.35	6.7	5
1987 May 4-5	0.99 ± 0.25	2.43 ± 0.08	2.16 ± 0.16	4.69 ± 0.38	6.7	6
<i>ASCA GIS</i> (0.6–11 keV)								
1993 Oct 6	...	0.76 ± 0.02	3.57 ± 0.24	13.5 ± 0.6	6.7	3
<i>Einstein SSS+MPC</i> (0.5–20 keV)								
1978 Apr 7	0.29 ± 0.002	...	1.46 ± 0.03	11.4 ± 0.2	5.5
	0.27	0.89	3.1	13.3 ± 0.7	...	5.5
<i>BeppoSAX LECS+MECS+HPGSPC+PDS</i> (0.3–40 keV)								
1998 Apr 17-18	0.1	0.47	0.55	4.5	2.9
1998 Sep 19-20								
	0.28 ± 0.03	0.46–0.66	2.83 ± 0.08	13.7 ± 0.5	...	3.7

^aOnly shown are fits using a cut-off power law or Comptonization (*CompST* in XSPEC) model, plus an option

^bHydrogen column density using cross sections of Morrison & McCammon (1983)

^cBlackbody temperature

^dCut-off power law photon index

^eCut-off power law cut-off energy

^fComptonizing electron temperature

^gComptonizing cloud optical depth

Table 2. *RXTE* Observations of 4U 1820-30

Date	Starting Time (MET) ^a	Mean Count Rate Cts s ⁻¹ PCU ⁻¹ (2–16 keV)
1996 Oct 26	88954464	434.3
1996 Oct 26	88977504	388.5
1996 Oct 28	89133104	481.4
1996 Oct 28	89161904	498.6
1996 Oct 30	89294096	655.2
1996 Oct 30	89322896	624.1
1996 Oct 30	89350464	551.2
1997 Feb 9	98100800	694.6
1997 Mar 6	100306640	785.8
1997 Mar 7	100312400	813.8
1997 Mar 21	101575104	540.6
1997 Mar 23	101753664	623.4
1997 Apr 10	103308800	491.3
1997 May 2	105199312	312.0
1997 May 10	105887120	616.3
1997 May 28	107432400	887.2
1997 Jun 23	109688672	855.2
1997 Jun 23	109707200	851.3
1997 Jul 16	111647472	819.9
1997 Jul 16	111670640	698.5
1997 Aug 15	114259928	752.7
1997 Sep 10	116477432	543.0
1997 Sep 10	116488824	562.5

^aMission Elapsed Time = seconds since 1994 Jan 1, 0h0m0s UTC

Table 3. Spectral Fits of 4U 1820-30 with the CPL + BB Model

S_a	Int Time (s)		kT_{BB} (keV)	R_{BB}^a (km)	α	E_c (keV)	E_l (keV)	Eqw ^b (eV)	L^c	L_{BB}/L_H	χ^2
	PCA	HEXTE									
1.03 ^d	8481	2803	2.57 ^{+0.04} _{-0.04}	0.88 ^{+0.04} _{-0.03}	2.05 ^{+0.05} _{-0.04}	23.07 ^{+2.91} _{-2.36}	6.53 ^{+0.12} _{-0.14}	89	2.31	0.26	0.0
1.21	4195	1362	2.37 ^{+0.05} _{-0.03}	1.17 ^{+0.04} _{-0.05}	2.00 ^{+0.06} _{-0.06}	11.56 ^{+1.20} _{-1.16}	6.82 ^{+0.14} _{-0.15}	76	2.63	0.29	0.0
1.23	5908	1874	2.41 ^{+0.05} _{-0.03}	1.25 ^{+0.04} _{-0.04}	1.86 ^{+0.05} _{-0.07}	8.48 ^{+0.63} _{-0.76}	6.84 ^{+0.16} _{-0.16}	70	2.74	0.30	0.0
1.25	3519	1229	2.40 ^{+0.04} _{-0.04}	1.24 ^{+0.04} _{-0.05}	1.84 ^{+0.06} _{-0.07}	8.25 ^{+0.73} _{-0.75}	6.87 ^{+0.18} _{-0.17}	57	2.84	0.31	0.0
1.28	9654	3174	2.48 ^{+0.04} _{-0.04}	1.22 ^{+0.03} _{-0.03}	1.54 ^{+0.06} _{-0.06}	5.68 ^{+0.44} _{-0.44}	6.93 ^{+0.18} _{-0.18}	33	3.12	0.29	0.0
1.30	13763	4268	2.41 ^{+0.04} _{-0.02}	1.21 ^{+0.04} _{-0.03}	1.55 ^{+0.05} _{-0.05}	6.12 ^{+0.31} _{-0.30}	6.79 ^{+0.18} _{-0.18}	27	3.22	0.26	0.0
1.32	15425	5006	2.51 ^{+0.05} _{-0.04}	1.17 ^{+0.03} _{-0.03}	1.43 ^{+0.05} _{-0.07}	5.25 ^{+0.36} _{-0.37}	6.88 ^{+0.18} _{-0.17}	45	3.23	0.27	0.0
1.35	9938	2982	2.57 ^{+0.05} _{-0.02}	1.13 ^{+0.03} _{-0.03}	1.32 ^{+0.03} _{-0.06}	4.86 ^{+0.38} _{-0.49}	6.83 ^{+0.16} _{-0.16}	33	3.55	0.26	0.0
1.38	6985	1268	2.58 ^{+0.05} _{-0.06}	1.10 ^{+0.05} _{-0.03}	1.28 ^{+0.07} _{-0.11}	4.67 ^{+0.47} _{-0.65}	6.88 ^{+0.15} _{-0.15}	50	3.38	0.27	0.0
1.40	10203	3130	2.56 ^{+0.05} _{-0.05}	1.15 ^{+0.03} _{-0.03}	1.27 ^{+0.05} _{-0.06}	4.90 ^{+0.31} _{-0.36}	6.78 ^{+0.16} _{-0.15}	30	3.77	0.24	0.0
1.42	3333	1029	2.43 ^{+0.07} _{-0.07}	1.13 ^{+0.05} _{-0.02}	1.34 ^{+0.06} _{-0.06}	5.52 ^{+0.37} _{-0.40}	6.85 ^{+0.15} _{-0.15}	53	3.31	0.22	0.0
1.45	2546	855	2.65 ^{+0.04} _{-0.08}	1.11 ^{+0.18} _{-0.05}	1.14 ^{+0.09} _{-0.19}	4.36 ^{+0.30} _{-1.02}	6.90 ^{+0.16} _{-0.16}	43	3.79	0.25	0.0
1.51	1840	604	2.65 ^{+0.04} _{-0.10}	1.15 ^{+0.21} _{-0.07}	1.04 ^{+0.10} _{-0.18}	4.11 ^{+0.62} _{-0.90}	6.85 ^{+0.14} _{-0.15}	55	4.29	0.24	0.0
1.54	6145	1912	2.54 ^{+0.07} _{-0.07}	1.10 ^{+0.05} _{-0.04}	1.15 ^{+0.06} _{-0.07}	4.80 ^{+0.32} _{-0.40}	6.86 ^{+0.16} _{-0.16}	62	3.67	0.21	0.0
1.56	10123	3135	2.44 ^{+0.06} _{-0.06}	1.15 ^{+0.06} _{-0.05}	1.17 ^{+0.05} _{-0.05}	5.10 ^{+0.22} _{-0.23}	6.82 ^{+0.14} _{-0.14}	50	4.10	0.19	0.0
1.57	7844	2301	2.53 ^{+0.07} _{-0.07}	1.11 ^{+0.05} _{-0.04}	1.12 ^{+0.06} _{-0.06}	4.82 ^{+0.29} _{-0.33}	6.80 ^{+0.15} _{-0.17}	58	4.19	0.20	0.0
1.60	5008	1638	2.48 ^{+0.08} _{-0.07}	1.09 ^{+0.07} _{-0.06}	1.12 ^{+0.05} _{-0.05}	5.03 ^{+0.24} _{-0.27}	6.85 ^{+0.15} _{-0.15}	45	4.34	0.17	0.0
1.63	566	184	2.61 ^{+0.02} _{-0.11}	1.09 ^{+0.08} _{-0.07}	0.98 ^{+0.07} _{-0.01}	4.31 ^{+0.43} _{-0.01}	6.82 ^{+0.15} _{-0.14}	45	4.79	0.20	0.0
1.65	5417	1668	2.62 ^{+0.06} _{-0.09}	1.14 ^{+0.12} _{-0.05}	0.98 ^{+0.07} _{-0.07}	4.24 ^{+0.39} _{-0.70}	6.93 ^{+0.19} _{-0.20}	71	4.14	0.22	0.0
1.67	15967	5063	2.46 ^{+0.06} _{-0.05}	1.20 ^{+0.06} _{-0.05}	1.04 ^{+0.05} _{-0.05}	4.68 ^{+0.18} _{-0.19}	6.74 ^{+0.12} _{-0.13}	51	4.71	0.19	0.0
1.70	9511	2962	2.42 ^{+0.07} _{-0.06}	1.17 ^{+0.07} _{-0.06}	1.03 ^{+0.05} _{-0.05}	4.82 ^{+0.19} _{-0.19}	6.75 ^{+0.15} _{-0.16}	55	4.78	0.17	0.0
1.73	9645	3200	2.54 ^{+0.08} _{-0.07}	1.17 ^{+0.04} _{-0.04}	0.94 ^{+0.05} _{-0.09}	4.26 ^{+0.25} _{-0.43}	6.82 ^{+0.15} _{-0.16}	74	4.45	0.21	0.0
1.75	3363	1030	2.56 ^{+0.08} _{-0.10}	1.20 ^{+0.05} _{-0.05}	0.94 ^{+0.07} _{-0.13}	4.24 ^{+0.39} _{-0.73}	6.92 ^{+0.18} _{-0.24}	77	4.06	0.23	0.0
1.77	8527	2708	2.48 ^{+0.09} _{-0.08}	1.09 ^{+0.08} _{-0.06}	0.92 ^{+0.05} _{-0.05}	4.47 ^{+0.20} _{-0.23}	6.77 ^{+0.12} _{-0.14}	69	4.85	0.16	0.0
1.80	5726	1812	2.53 ^{+0.09} _{-0.09}	1.14 ^{+0.06} _{-0.05}	0.87 ^{+0.06} _{-0.08}	4.21 ^{+0.26} _{-0.40}	6.75 ^{+0.15} _{-0.19}	90	4.61	0.19	0.0
1.82	10348	3097	2.50 ^{+0.07} _{-0.07}	1.24 ^{+0.06} _{-0.05}	0.91 ^{+0.05} _{-0.06}	4.35 ^{+0.22} _{-0.27}	6.82 ^{+0.15} _{-0.17}	60	4.90	0.21	0.0
1.85	6401	1964	2.45 ^{+0.08} _{-0.08}	1.24 ^{+0.08} _{-0.06}	0.88 ^{+0.06} _{-0.06}	4.40 ^{+0.20} _{-0.25}	6.76 ^{+0.15} _{-0.18}	68	5.10	0.19	0.0
1.87 ^c	466	161	2.44 ^{+0.15} _{-0.14}	1.47 ^{+0.16} _{-0.11}	0.89 ^{+0.09} _{-0.13}	4.41 ^{+0.42} _{-0.72}	6.80 ^{+0.00} _{-0.00}	47	5.54	0.20	0.0
1.91	3327	1001	2.52 ^{+0.06} _{-0.05}	1.51 ^{+0.05} _{-0.04}	1.05 ^{+0.07} _{-0.07}	4.64 ^{+0.33} _{-0.41}	6.78 ^{+0.16} _{-0.16}	43	5.25	0.30	0.0
1.93	3347	1023	2.51 ^{+0.05} _{-0.05}	1.54 ^{+0.05} _{-0.05}	1.03 ^{+0.06} _{-0.07}	4.68 ^{+0.29} _{-0.34}	6.73 ^{+0.15} _{-0.15}	32	5.29	0.29	0.0
1.96	3502	1015	2.62 ^{+0.03} _{-0.05}	1.50 ^{+0.15} _{-0.06}	0.86 ^{+0.09} _{-0.15}	3.88 ^{+0.47} _{-0.70}	6.80 ^{+0.00} _{-0.00}	51	5.39	0.33	0.0
2.00	3510	1037	2.59 ^{+0.04} _{-0.06}	1.61 ^{+0.40} _{-0.04}	0.99 ^{+0.09} _{-0.09}	4.20 ^{+0.73} _{-1.74}	6.89 ^{+0.21} _{-0.20}	32	5.29	0.37	0.0

^aBlackbody radius

^bGaussian line equivalent width

^cTotal luminosity, $\times 10^{37}$ ergs s⁻¹, for a distance of 6.4 kpc, 2–50 keV. This is the raw luminosity derived from fit.

^dSmearred edge included at 8.90^{+0.42}_{-0.38} keV

Table 4. Spectral Fits of 4U 1820-30 with the CompTT + BB Model

S_a	kT_{BB} (keV)	R_{BB} (km)	τ	kT_e (keV)	kT_W^a (keV)	y^b	R_W^c (km)	Eqw (eV)	L^d	L_{BB}/L_H	χ
1.03 ^e	2.41 ^{+0.03} _{-0.04}	1.00 ^{+0.03} _{-0.06}	6.00 ^{+0.38} _{-0.52}	7.94 ^{+1.01} _{-0.65}	0.38 ^{+0.05} _{-0.06}	2.24	44.63 ^{+12.45} _{-14.35}	55	2.31	0.36	0.
1.21	2.28 ^{+0.02} _{-0.02}	1.26 ^{+0.04} _{-0.05}	7.37 ^{+0.93} _{-0.79}	4.88 ^{+0.68} _{-0.58}	0.45 ^{+0.02} _{-0.03}	2.08	33.27 ^{+4.60} _{-5.75}	82	2.60	0.42	0.
1.23	2.30 ^{+0.03} _{-0.02}	1.33 ^{+0.07} _{-0.08}	8.45 ^{+0.82} _{-0.93}	3.99 ^{+0.48} _{-0.32}	0.47 ^{+0.03} _{-0.03}	2.23	30.96 ^{+4.13} _{-4.60}	79	2.71	0.40	0.
1.25	2.29 ^{+0.03} _{-0.03}	1.32 ^{+0.09} _{-0.08}	8.45 ^{+0.87} _{-1.48}	3.96 ^{+0.85} _{-0.33}	0.47 ^{+0.03} _{-0.03}	2.21	30.78 ^{+4.83} _{-5.20}	72	2.81	0.42	0.
1.28	2.32 ^{+0.05} _{-0.04}	1.26 ^{+0.14} _{-0.16}	9.85 ^{+1.02} _{-1.10}	3.31 ^{+0.31} _{-0.22}	0.51 ^{+0.03} _{-0.03}	2.51	27.36 ^{+3.57} _{-3.69}	64	3.08	0.31	0.
1.30	2.28 ^{+0.02} _{-0.03}	1.55 ^{+0.03} _{-0.14}	6.38 ^{+2.42} _{-1.46}	4.89 ^{+1.61} _{-1.25}	0.58 ^{+0.01} _{-0.04}	1.56	23.42 ^{+5.97} _{-5.01}	92	3.18	0.54	0.
1.32	2.31 ^{+0.11} _{-0.05}	1.09 ^{+0.17} _{-0.27}	10.95 ^{+1.20} _{-0.90}	3.09 ^{+0.17} _{-0.18}	0.51 ^{+0.02} _{-0.03}	2.90	27.78 ^{+3.36} _{-4.14}	68	3.20	0.21	0.
1.35	2.33 ^{+0.09} _{-0.04}	1.23 ^{+0.21} _{-0.29}	10.03 ^{+1.54} _{-1.52}	3.24 ^{+0.41} _{-0.27}	0.55 ^{+0.02} _{-0.03}	2.55	25.03 ^{+3.64} _{-4.11}	77	3.51	0.27	0.
1.38	2.34 ^{+0.63} _{-0.09}	0.91 ^{+0.31} _{-0.35}	11.65 ^{+1.51} _{-1.23}	2.98 ^{+0.21} _{-1.16}	0.52 ^{+0.02} _{-0.03}	3.17	26.96 ^{+3.16} _{-5.49}	77	3.35	0.14	0.
1.40	2.29 ^{+0.06} _{-0.04}	1.35 ^{+0.17} _{-0.37}	9.90 ^{+1.98} _{-1.25}	3.30 ^{+0.33} _{-0.34}	0.57 ^{+0.02} _{-0.04}	2.53	24.45 ^{+4.08} _{-3.84}	80	3.73	0.28	0.
1.42	2.12 ^{+0.06} _{-0.15}	1.26 ^{+0.19} _{-0.29}	10.99 ^{+1.45} _{-1.29}	3.17 ^{+0.29} _{-0.23}	0.52 ^{+0.03} _{-0.03}	3.00	26.20 ^{+3.92} _{-4.17}	80	3.27	0.19	0.
1.45	2.24 ^{+0.26} _{-0.47}	0.91 ^{+0.48} _{-0.45}	11.95 ^{+1.21} _{-1.58}	2.98 ^{+0.26} _{-0.17}	0.54 ^{+0.03} _{-0.04}	3.34	26.28 ^{+3.44} _{-4.75}	76	3.76	0.09	0.
1.51	1.35 ^{+0.65} _{-0.34}	1.36 ^{+3.38} _{-0.60}	13.30 ^{+0.54} _{-0.71}	2.82 ^{+0.08} _{-0.04}	0.52 ^{+0.03} _{-0.04}	3.90	29.68 ^{+3.14} _{-5.19}	76	4.26	0.02	0.
1.54	1.72 ^{+0.31} _{-0.36}	1.13 ^{+0.63} _{-0.22}	13.06 ^{+0.51} _{-1.02}	2.88 ^{+0.13} _{-0.06}	0.51 ^{+0.03} _{-0.03}	3.84	28.01 ^{+3.33} _{-3.91}	71	3.64	0.05	0.
1.56	2.01 ^{+0.10} _{-0.21}	1.45 ^{+0.16} _{-0.16}	11.56 ^{+1.10} _{-1.24}	3.09 ^{+0.22} _{-0.16}	0.55 ^{+0.02} _{-0.03}	3.23	26.11 ^{+3.12} _{-3.60}	82	4.06	0.16	0.
1.57	1.71 ^{+0.40} _{-0.37}	1.20 ^{+0.85} _{-0.24}	13.05 ^{+0.55} _{-1.78}	2.88 ^{+0.24} _{-0.06}	0.52 ^{+0.04} _{-0.04}	3.84	28.47 ^{+4.75} _{-4.98}	75	4.16	0.05	0.
1.60	1.94 ^{+0.15} _{-0.28}	1.45 ^{+0.17} _{-0.16}	11.87 ^{+1.04} _{-1.36}	3.06 ^{+0.24} _{-0.15}	0.55 ^{+0.03} _{-0.03}	3.38	26.54 ^{+3.41} _{-3.90}	75	4.30	0.13	0.
1.63	2.02 ^{+0.48} _{-2.02}	1.16 ^{+0.69} _{-0.58}	12.34 ^{+1.70} _{-2.90}	2.93 ^{+0.54} _{-0.16}	0.58 ^{+0.04} _{-0.06}	3.49	25.56 ^{+4.64} _{-6.83}	92	4.74	0.09	0.
1.65	1.62 ^{+0.31} _{-0.27}	1.45 ^{+0.77} _{-0.28}	13.38 ^{+0.50} _{-0.84}	2.84 ^{+0.10} _{-0.05}	0.53 ^{+0.03} _{-0.03}	3.98	27.32 ^{+2.83} _{-3.77}	70	4.11	0.05	0.
1.67	2.03 ^{+0.11} _{-0.44}	1.51 ^{+0.23} _{-0.22}	11.82 ^{+1.68} _{-1.55}	3.01 ^{+0.25} _{-0.20}	0.58 ^{+0.03} _{-0.05}	3.29	25.12 ^{+3.81} _{-4.85}	94	4.66	0.16	0.
1.70	2.01 ^{+0.12} _{-0.26}	1.68 ^{+0.19} _{-0.16}	11.33 ^{+1.53} _{-2.03}	3.12 ^{+0.43} _{-0.22}	0.58 ^{+0.04} _{-0.04}	3.14	24.74 ^{+4.16} _{-4.69}	92	4.73	0.20	0.
1.73	1.44 ^{+0.19} _{-0.17}	1.92 ^{+0.93} _{-0.41}	14.07 ^{+0.45} _{-0.40}	2.76 ^{+0.04} _{-0.03}	0.52 ^{+0.03} _{-0.04}	4.27	28.85 ^{+3.00} _{-4.74}	76	4.42	0.06	0.
1.75	1.57 ^{+0.23} _{-0.18}	1.78 ^{+0.48} _{-0.31}	13.95 ^{+0.45} _{-0.73}	2.80 ^{+0.08} _{-0.05}	0.51 ^{+0.03} _{-0.03}	4.26	27.89 ^{+3.36} _{-3.89}	62	4.04	0.07	0.
1.77	1.50 ^{+0.19} _{-0.13}	2.26 ^{+0.60} _{-0.40}	13.75 ^{+0.47} _{-0.62}	2.81 ^{+0.06} _{-0.04}	0.52 ^{+0.03} _{-0.04}	4.16	29.17 ^{+3.88} _{-4.47}	76	4.82	0.10	0.
1.80	1.43 ^{+0.13} _{-0.12}	2.47 ^{+0.65} _{-0.40}	14.28 ^{+0.45} _{-0.43}	2.76 ^{+0.04} _{-0.04}	0.50 ^{+0.03} _{-0.04}	4.40	29.98 ^{+3.76} _{-5.28}	75	4.59	0.09	0.
1.82	1.53 ^{+0.25} _{-0.16}	1.96 ^{+0.67} _{-0.38}	14.17 ^{+0.47} _{-0.70}	2.77 ^{+0.07} _{-0.04}	0.52 ^{+0.03} _{-0.04}	4.35	28.98 ^{+3.74} _{-4.36}	66	4.88	0.07	0.
1.85	1.51 ^{+0.19} _{-0.13}	2.31 ^{+0.62} _{-0.40}	14.23 ^{+0.49} _{-0.67}	2.77 ^{+0.06} _{-0.04}	0.52 ^{+0.03} _{-0.04}	4.39	29.55 ^{+4.06} _{-4.68}	69	5.05	0.10	0.
1.87 ^f	1.98 ^{+0.15} _{-0.41}	2.16 ^{+0.36} _{-0.46}	12.00 ^{+2.34} _{-3.35}	3.03 ^{+0.77} _{-0.27}	0.59 ^{+0.05} _{-0.05}	3.41	25.41 ^{+6.01} _{-7.15}	70	5.54	0.22	0.
1.91	2.15 ^{+0.35} _{-2.15}	0.92 ^{+0.84} _{-0.46}	14.27 ^{+1.03} _{-2.08}	2.81 ^{+0.22} _{-0.07}	0.53 ^{+0.04} _{-0.06}	4.48	29.30 ^{+4.54} _{-7.81}	66	5.20	0.06	0.
1.93	2.24 ^{+0.05} _{-0.18}	1.72 ^{+0.36} _{-0.62}	11.58 ^{+2.81} _{-2.70}	3.11 ^{+0.58} _{-0.31}	0.59 ^{+0.04} _{-0.05}	3.26	24.46 ^{+5.90} _{-5.99}	76	5.25	0.30	0.
1.96	1.30 ^{+1.20} _{-0.43}	1.47 ^{+3.24} _{-0.73}	15.21 ^{+0.61} _{-0.83}	2.75 ^{+0.06} _{-0.03}	0.53 ^{+0.06} _{-0.05}	4.97	29.27 ^{+6.96} _{-5.71}	60	5.34	0.02	0.
2.00	2.36 ^{+0.18} _{-0.04}	1.74 ^{+0.25} _{-0.61}	11.08 ^{+3.15} _{-1.94}	3.16 ^{+0.42} _{-1.03}	0.59 ^{+0.02} _{-0.05}	3.04	23.76 ^{+5.38} _{-5.98}	72	5.25	0.43	0.

^aTemperature of seed photons (assumed to follow a Wien law)

^bComptonization parameter $y = 4kT_e\tau^2/m_e c^2$

^cEquivalent Wien radius of seed photons (see text)

^dTotal luminosity, $\times 10^{37}$ ergs s^{-1} , for a distance of 6.4 kpc, 2–50 keV. This is the raw luminosity derived from fit.

Table 5. Spectral Fits of 4U 1820-30 with the CPL + DBB Model

S_a	kT_{in}^a (keV)	$R_{in}\sqrt{\cos\theta^b}$ (km)	α	E_c (keV)	E_l (keV)	Eqw (eV)	L^c	L_{DBB}/L_H	χ^2_ν
1.03	$0.58^{+0.04}_{-0.04}$	$15.55^{+3.66}_{-1.85}$	$0.83^{+0.04}_{-0.05}$	$6.58^{+0.13}_{-0.15}$	$6.86^{+0.22}_{-0.32}$	113	2.25	0.08	0.88
1.21	$0.72^{+0.04}_{-0.03}$	$11.99^{+1.20}_{-1.16}$	$0.25^{+0.06}_{-0.10}$	$4.26^{+0.09}_{-0.13}$	$6.75^{+0.14}_{-0.09}$	54	2.59	0.15	0.61
1.23	$0.82^{+0.05}_{-0.03}$	$10.33^{+0.68}_{-0.78}$	$-0.09^{+0.09}_{-0.17}$	$3.73^{+0.10}_{-0.16}$	$6.61^{+0.16}_{-0.30}$	91	2.71	0.20	0.55
1.25	$0.82^{+0.05}_{-0.03}$	$9.94^{+0.72}_{-0.82}$	$-0.11^{+0.09}_{-0.19}$	$3.67^{+0.10}_{-0.13}$	$6.64^{+0.18}_{-0.32}$	75	2.81	0.20	0.68
1.28	$0.93^{+0.04}_{-0.02}$	$8.77^{+0.40}_{-0.49}$	$-0.30^{+0.09}_{-0.17}$	$3.41^{+0.08}_{-0.13}$	$6.72^{+0.15}_{-0.22}$	65	3.10	0.25	0.40
1.30	$0.91^{+0.03}_{-0.03}$	$8.71^{+0.45}_{-0.40}$	$-0.17^{+0.09}_{-0.11}$	$3.51^{+0.09}_{-0.10}$	$6.66^{+0.16}_{-0.19}$	59	3.19	0.23	0.65
1.32	$0.96^{+0.05}_{-0.03}$	$8.15^{+0.34}_{-0.45}$	$-0.36^{+0.10}_{-0.21}$	$3.34^{+0.08}_{-0.15}$	$6.61^{+0.18}_{-0.36}$	102	3.21	0.26	0.38
1.35	$1.00^{+0.04}_{-0.02}$	$7.82^{+0.33}_{-0.35}$	$-0.35^{+0.11}_{-0.16}$	$3.36^{+0.09}_{-0.12}$	$6.70^{+0.15}_{-0.18}$	75	3.53	0.27	0.48
1.38	$1.00^{+0.05}_{-0.03}$	$7.57^{+0.17}_{-0.44}$	$-0.38^{+0.12}_{-0.24}$	$3.34^{+0.10}_{-0.18}$	$6.66^{+0.16}_{-0.28}$	108	3.37	0.27	0.51
1.40	$1.01^{+0.03}_{-0.03}$	$7.87^{+0.35}_{-0.32}$	$-0.29^{+0.11}_{-0.13}$	$3.41^{+0.09}_{-0.10}$	$6.69^{+0.14}_{-0.16}$	68	3.75	0.26	0.38
1.42	$0.91^{+0.06}_{-0.04}$	$8.19^{+0.53}_{-0.58}$	$0.00^{+0.11}_{-0.21}$	$3.66^{+0.11}_{-0.19}$	$6.73^{+0.14}_{-0.16}$	73	3.29	0.19	0.57
1.45	$1.02^{+0.06}_{-0.02}$	$7.63^{+0.35}_{-0.43}$	$-0.21^{+0.13}_{-0.26}$	$3.49^{+0.12}_{-0.21}$	$6.76^{+0.15}_{-0.19}$	75	3.78	0.24	0.54
1.51	$1.03^{+0.07}_{-0.05}$	$7.69^{+0.41}_{-0.40}$	$-0.21^{+0.18}_{-0.27}$	$3.45^{+0.16}_{-0.21}$	$6.70^{+0.15}_{-0.21}$	95	4.28	0.24	0.57
1.54	$0.99^{+0.06}_{-0.04}$	$7.57^{+0.38}_{-0.43}$	$-0.11^{+0.11}_{-0.22}$	$3.55^{+0.10}_{-0.18}$	$6.68^{+0.16}_{-0.25}$	97	3.65	0.21	0.49
1.56	$0.95^{+0.04}_{-0.02}$	$7.85^{+0.47}_{-0.38}$	$0.03^{+0.10}_{-0.12}$	$3.67^{+0.10}_{-0.11}$	$6.73^{+0.13}_{-0.16}$	74	4.08	0.18	0.37
1.57	$1.01^{+0.06}_{-0.04}$	$7.50^{+0.38}_{-0.41}$	$-0.14^{+0.11}_{-0.22}$	$3.53^{+0.10}_{-0.18}$	$6.64^{+0.17}_{-0.26}$	107	4.18	0.21	0.60
1.60	$0.96^{+0.06}_{-0.05}$	$7.53^{+0.45}_{-0.41}$	$0.09^{+0.10}_{-0.16}$	$3.75^{+0.11}_{-0.15}$	$6.76^{+0.15}_{-0.17}$	66	4.32	0.17	0.49
1.63	$1.05^{+0.11}_{-0.06}$	$7.08^{+0.45}_{-0.52}$	$-0.18^{+0.19}_{-0.45}$	$3.46^{+0.17}_{-0.33}$	$6.75^{+0.15}_{-0.17}$	77	4.77	0.22	0.87
1.65	$1.05^{+0.07}_{-0.04}$	$7.18^{+0.36}_{-0.42}$	$-0.26^{+0.12}_{-0.27}$	$3.41^{+0.10}_{-0.20}$	$6.70^{+0.20}_{-0.30}$	117	4.13	0.23	0.42
1.67	$1.00^{+0.05}_{-0.04}$	$7.46^{+0.39}_{-0.36}$	$-0.09^{+0.09}_{-0.14}$	$3.50^{+0.08}_{-0.11}$	$6.68^{+0.13}_{-0.17}$	80	4.69	0.19	0.54
1.70	$0.99^{+0.06}_{-0.05}$	$7.28^{+0.43}_{-0.39}$	$-0.00^{+0.10}_{-0.15}$	$3.60^{+0.10}_{-0.13}$	$6.67^{+0.15}_{-0.21}$	85	4.76	0.17	0.55
1.73	$1.06^{+0.07}_{-0.04}$	$6.90^{+0.37}_{-0.41}$	$-0.32^{+0.12}_{-0.26}$	$3.31^{+0.09}_{-0.18}$	$6.64^{+0.17}_{-0.31}$	127	4.43	0.23	0.41
1.75	$1.03^{+0.10}_{-0.05}$	$7.09^{+0.41}_{-0.53}$	$-0.23^{+0.14}_{-0.35}$	$3.40^{+0.12}_{-0.25}$	$6.71^{+0.20}_{-0.40}$	106	4.06	0.20	0.53
1.77	$1.01^{+0.07}_{-0.05}$	$6.82^{+0.43}_{-0.37}$	$-0.01^{+0.11}_{-0.19}$	$3.56^{+0.10}_{-0.15}$	$6.67^{+0.14}_{-0.21}$	98	4.84	0.16	0.48
1.80	$1.04^{+0.09}_{-0.05}$	$6.82^{+0.45}_{-0.43}$	$-0.18^{+0.12}_{-0.27}$	$3.40^{+0.10}_{-0.20}$	$6.59^{+0.17}_{-0.31}$	128	4.61	0.19	0.38
1.82	$1.04^{+0.08}_{-0.04}$	$6.99^{+0.39}_{-0.42}$	$-0.23^{+0.11}_{-0.22}$	$3.37^{+0.09}_{-0.16}$	$6.68^{+0.17}_{-0.31}$	95	4.90	0.19	0.40
1.85	$1.02^{+0.08}_{-0.05}$	$7.02^{+0.22}_{-0.44}$	$-0.13^{+0.11}_{-0.21}$	$3.44^{+0.09}_{-0.16}$	$6.65^{+0.16}_{-0.26}$	96	5.10	0.17	0.45
1.87 ^d	$1.14^{+0.09}_{-0.15}$	$7.27^{+0.91}_{-0.72}$	$-0.48^{+0.37}_{-0.46}$	$3.18^{+0.29}_{-0.16}$	$6.94^{+0.29}_{-0.43}$	110	5.54	0.24	0.63
1.91	$1.06^{+0.07}_{-0.04}$	$7.45^{+0.40}_{-0.52}$	$-0.55^{+0.11}_{-0.23}$	$3.22^{+0.08}_{-0.15}$	$6.68^{+0.16}_{-0.23}$	74	5.25	0.22	0.58
1.93	$1.05^{+0.06}_{-0.04}$	$7.50^{+0.39}_{-0.45}$	$-0.48^{+0.10}_{-0.16}$	$3.26^{+0.07}_{-0.12}$	$6.68^{+0.14}_{-0.15}$	51	5.29	0.21	0.55
1.96	$1.19^{+0.08}_{-0.08}$	$6.39^{+0.52}_{-0.43}$	$-0.88^{+0.26}_{-0.26}$	$3.02^{+0.16}_{-0.14}$	$6.69^{+0.24}_{-0.41}$	116	5.39	0.28	0.47
2.00	$1.13^{+0.08}_{-0.04}$	$6.86^{+0.36}_{-0.56}$	$-0.83^{+0.12}_{-0.28}$	$3.07^{+0.08}_{-0.16}$	$6.80^{+0.19}_{-0.24}$	65	5.29	0.25	0.60

^aDisk inner temperature

^bDisk inner radius

^cTotal luminosity, $\times 10^{37}$ ergs s^{-1} , for a distance of 6.4 kpc, 2–50 keV. This is the raw luminosity derived from the fit.

^dOnly PCUs 0 and 1 available

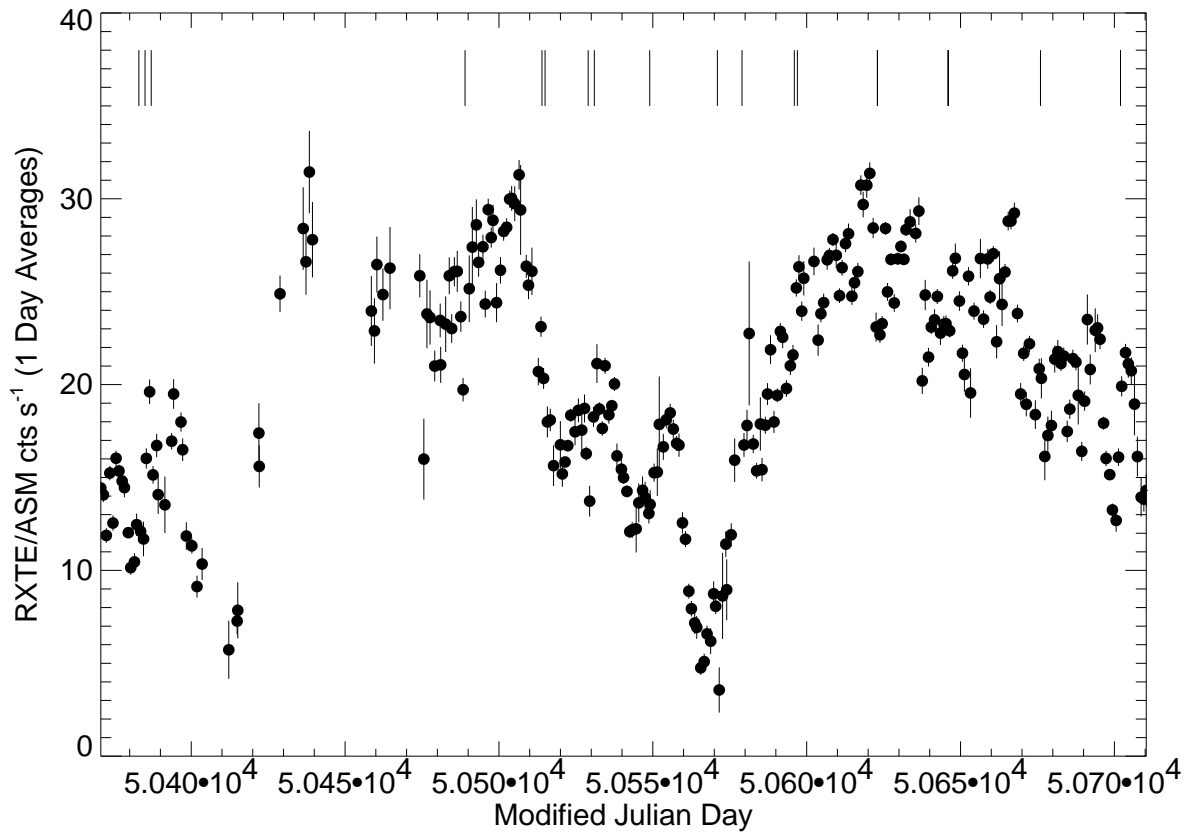


Fig. 1.—

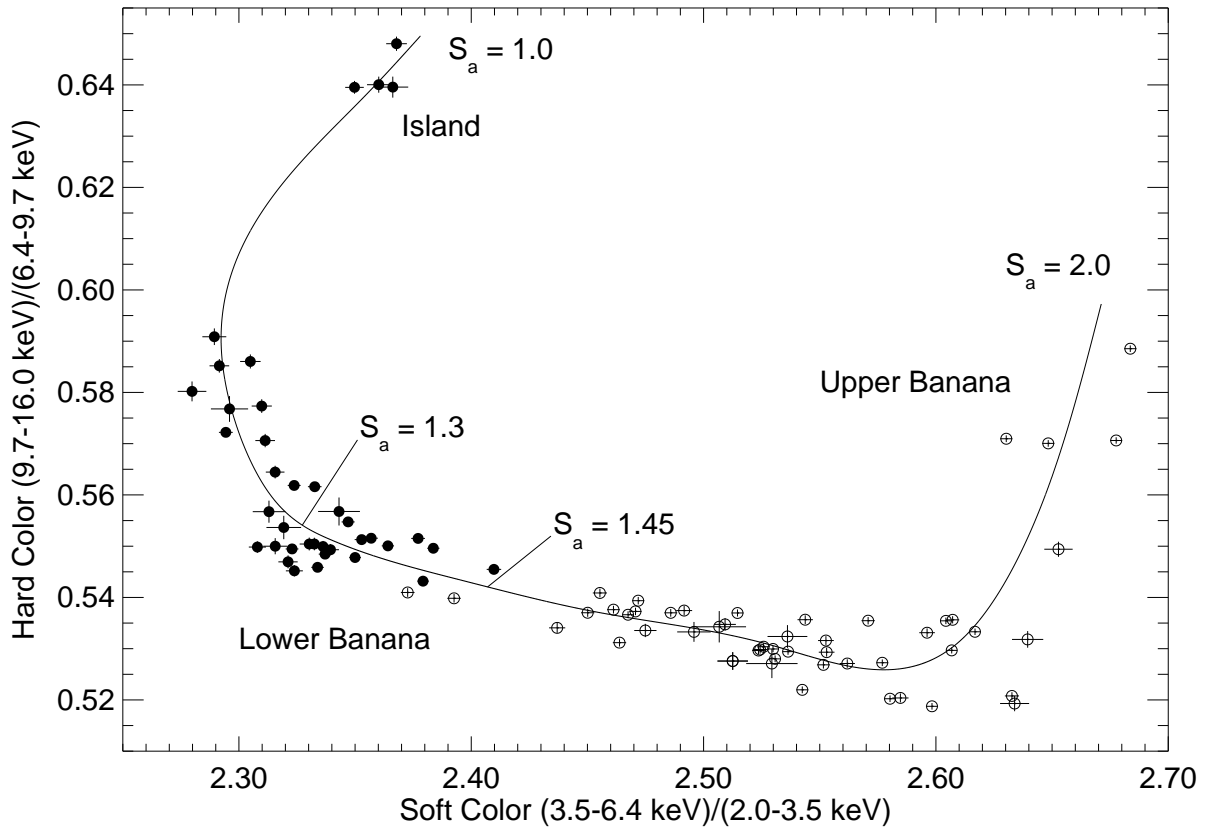


Fig. 2.—

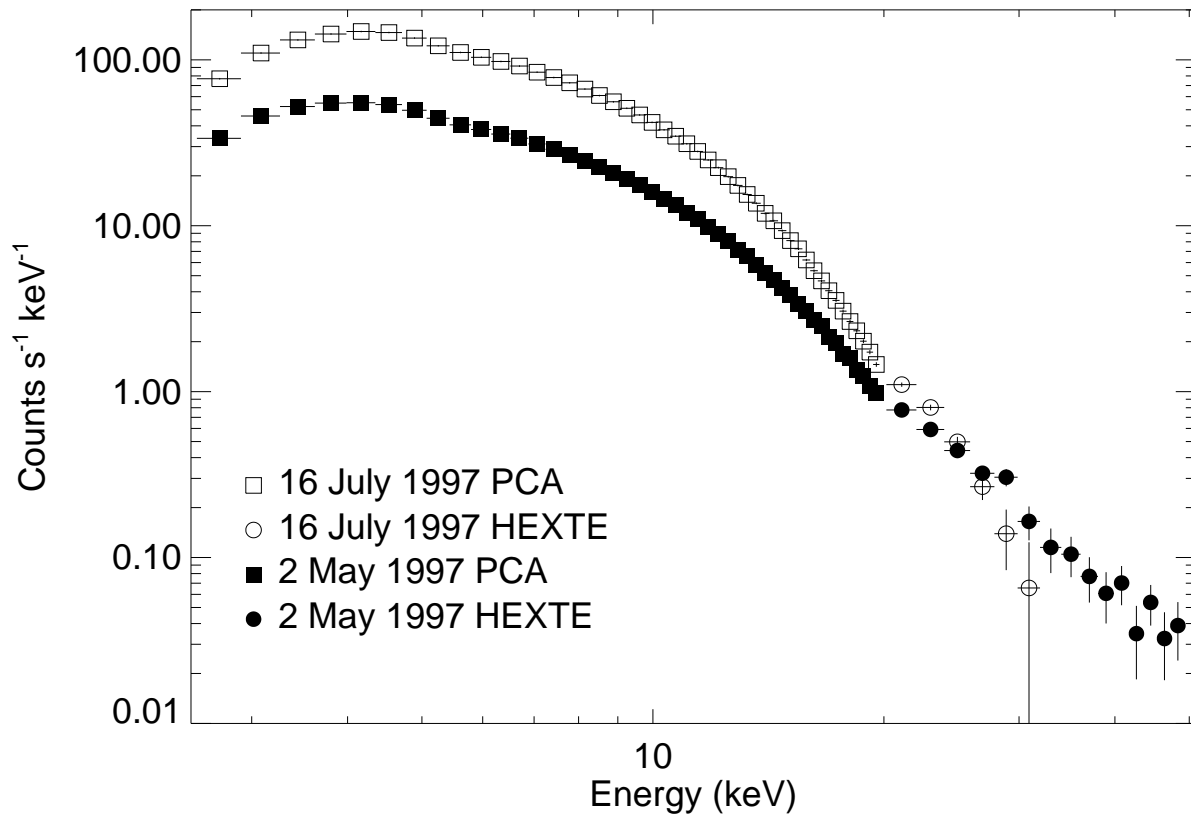


Fig. 3.—

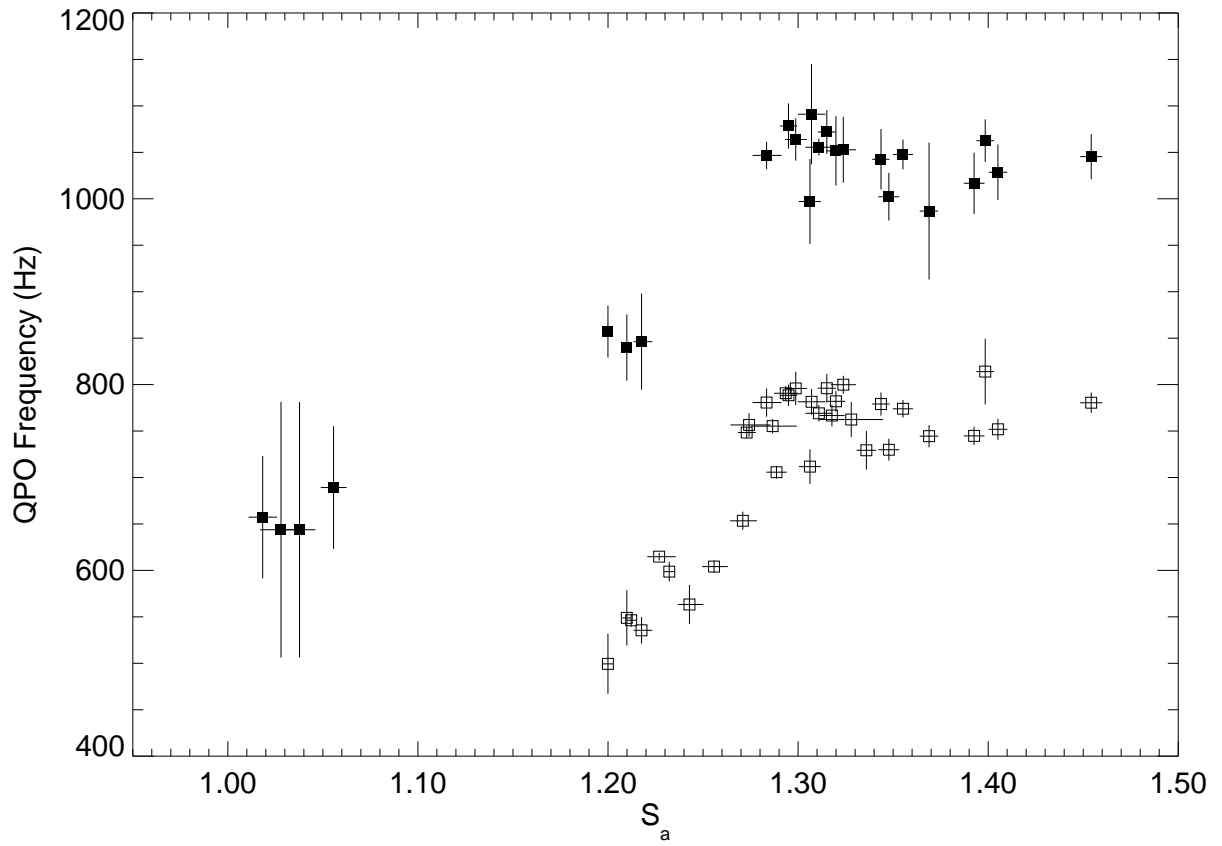


Fig. 4.—

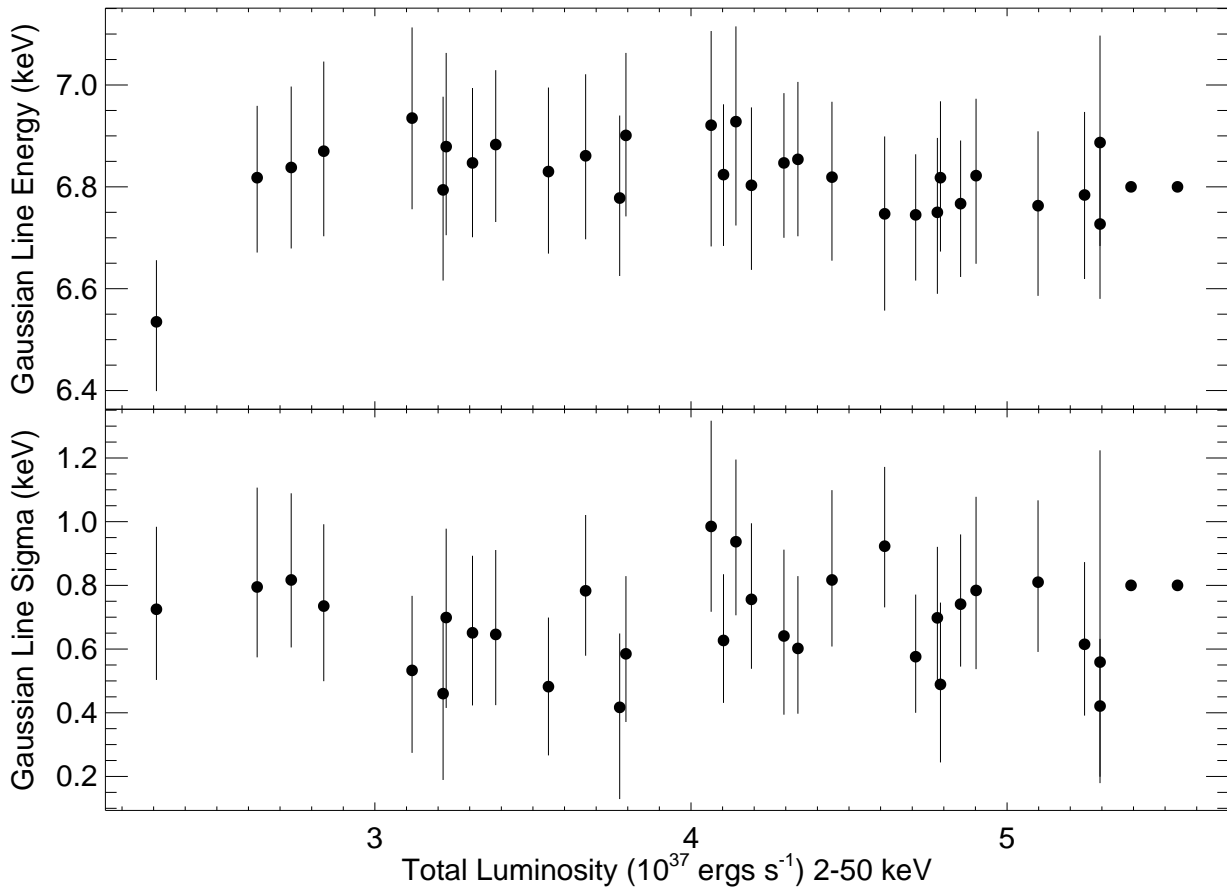


Fig. 5.—

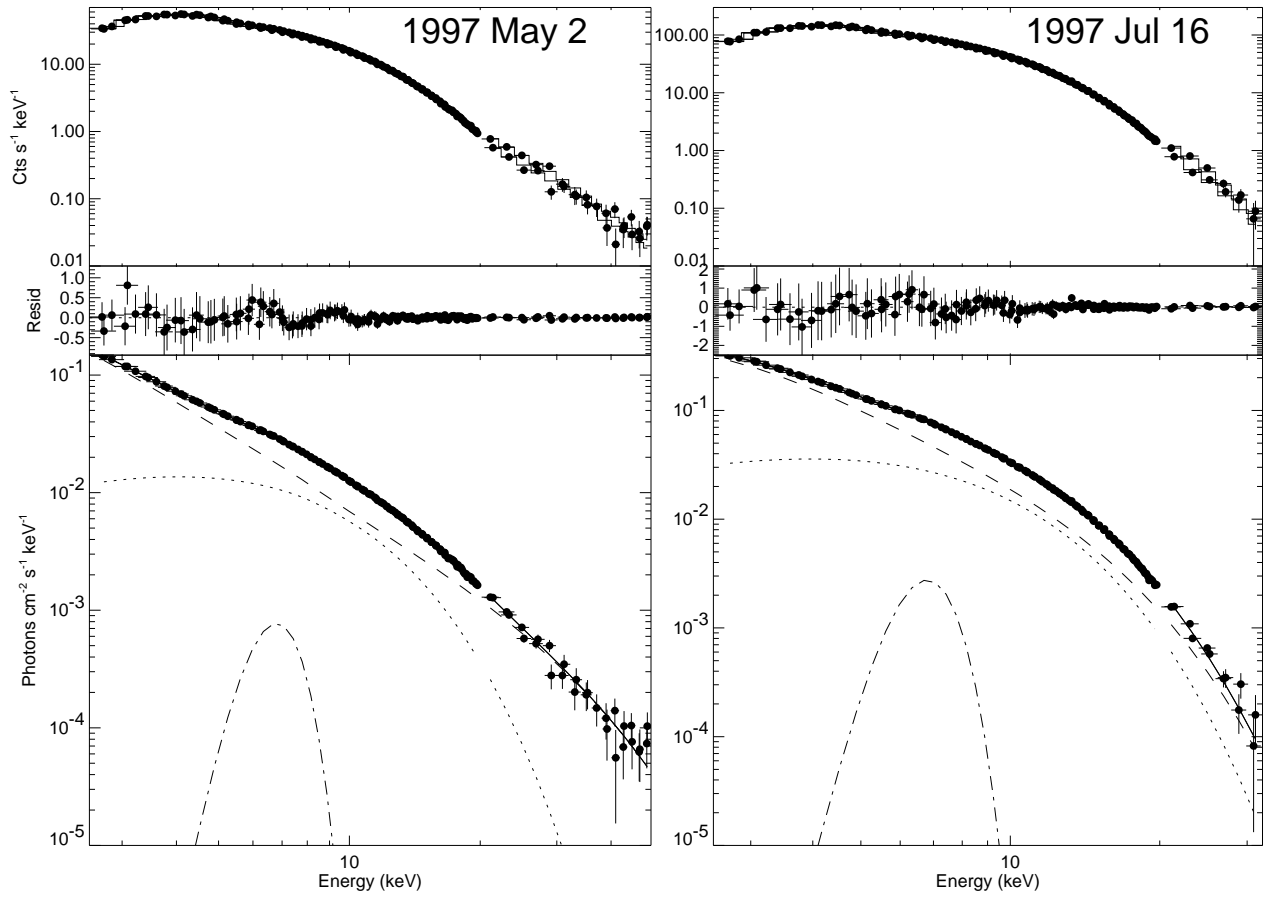


Fig. 6.—

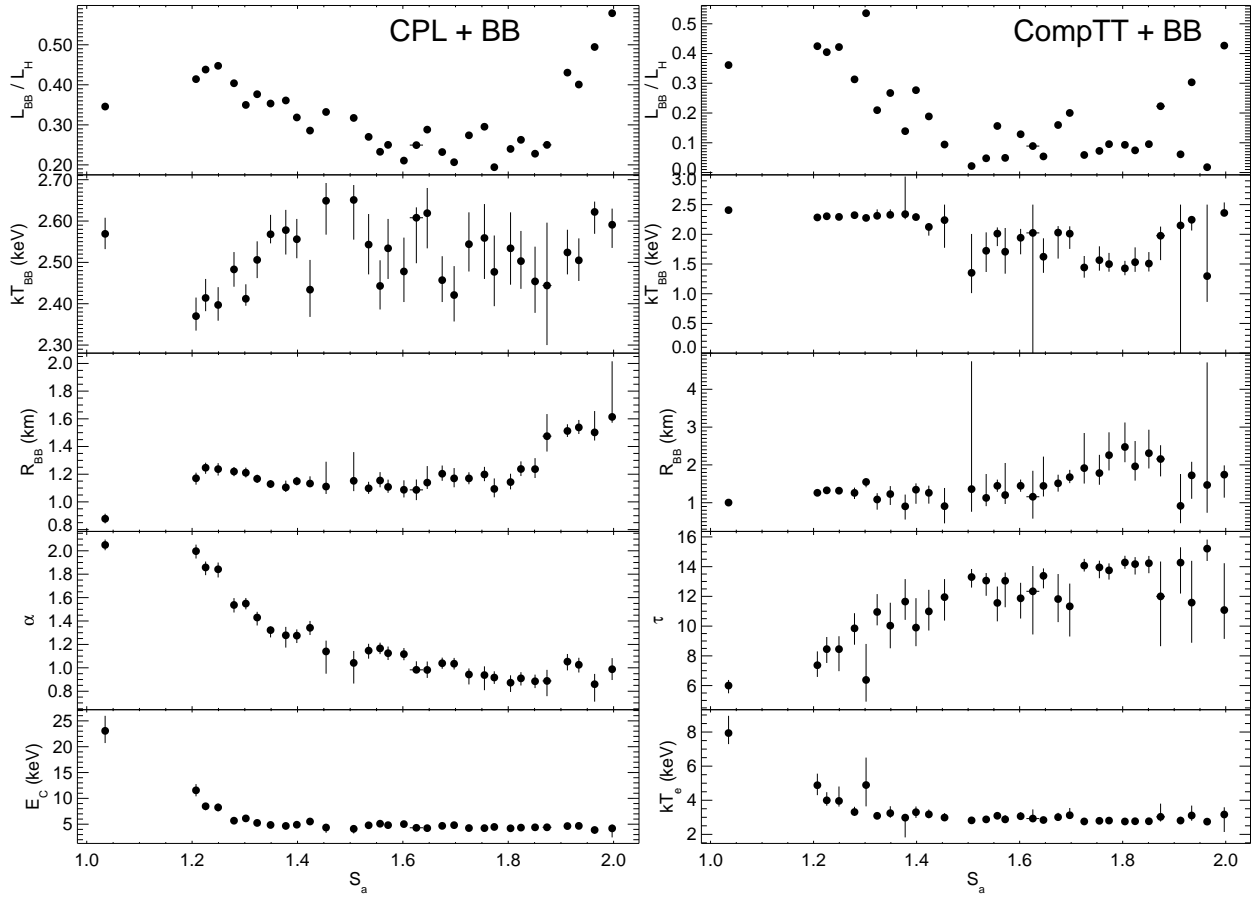


Fig. 7.—

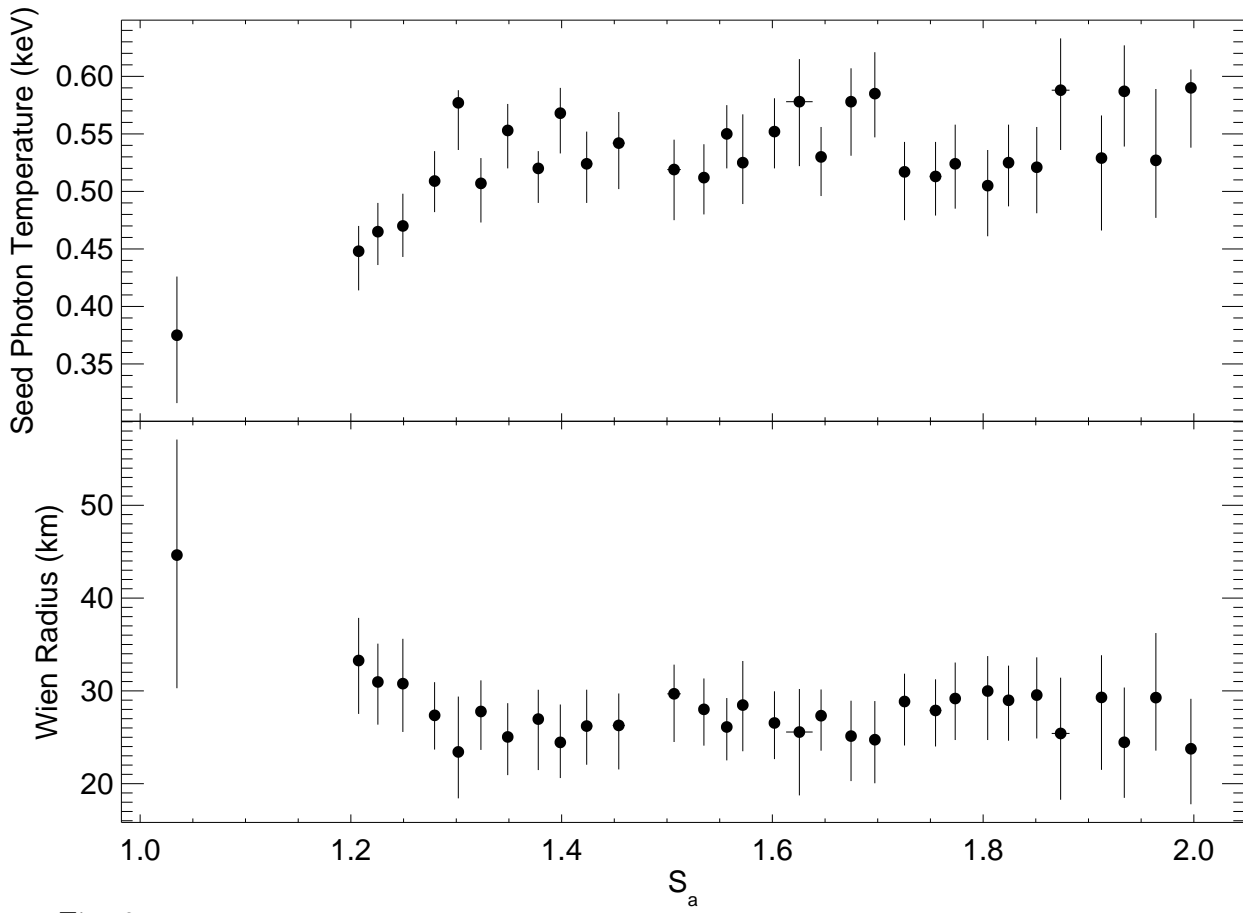


Fig. 8.—

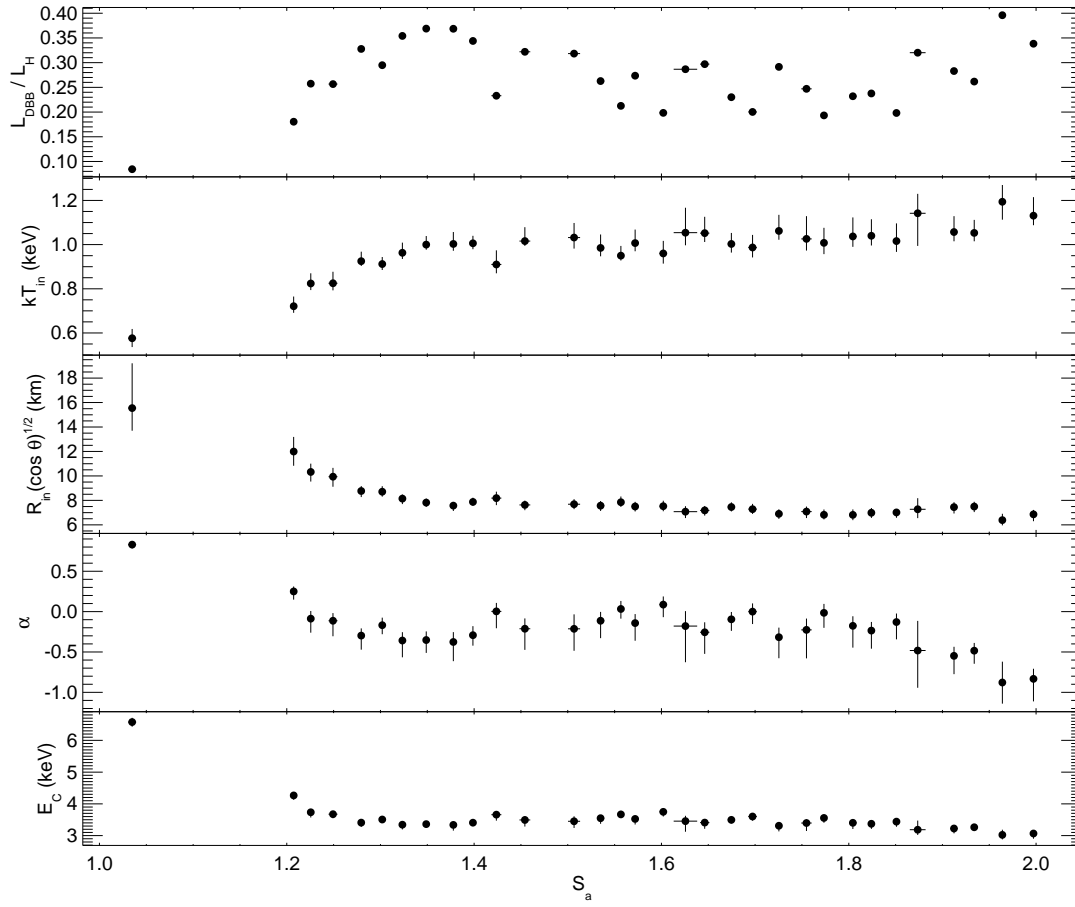


Fig. 9.—

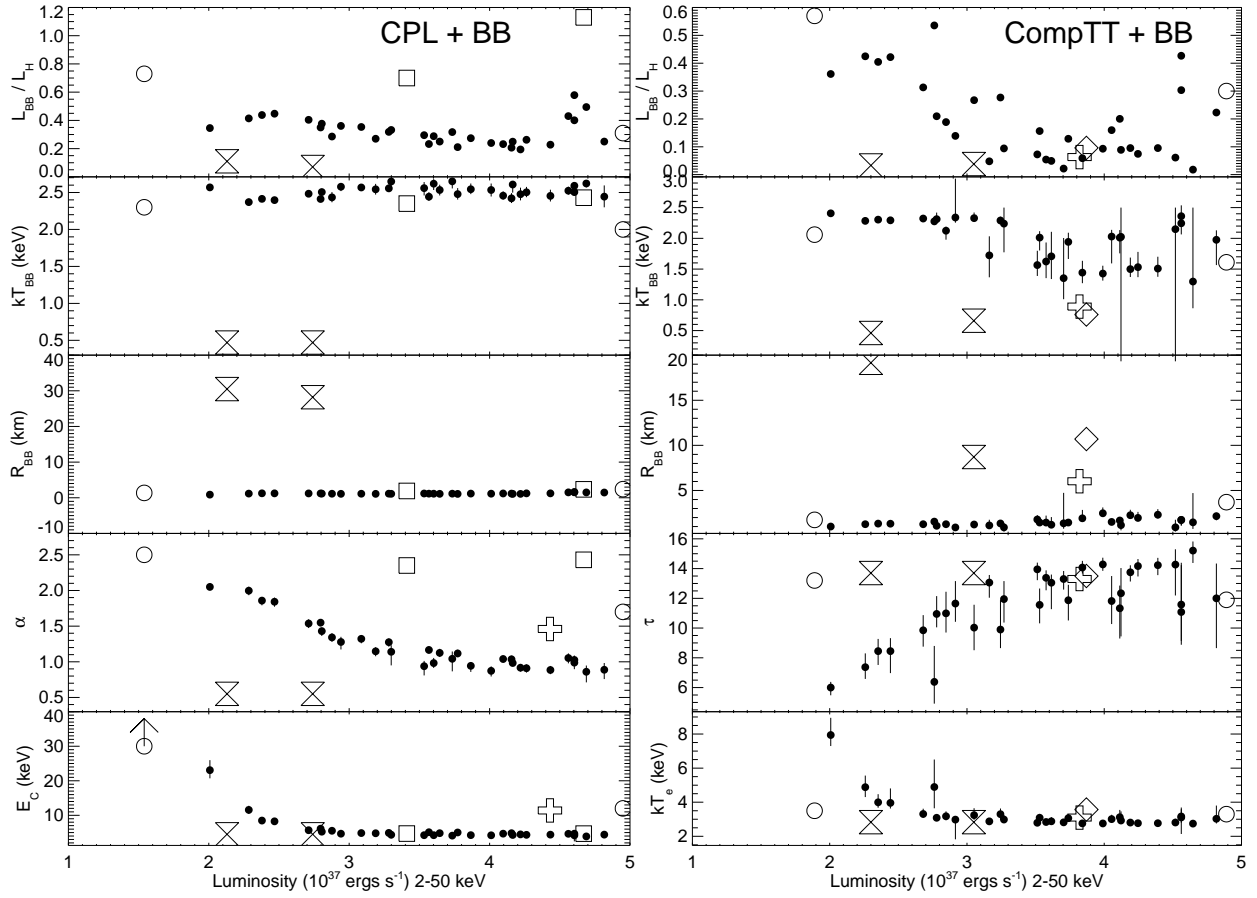


Fig. 10.—

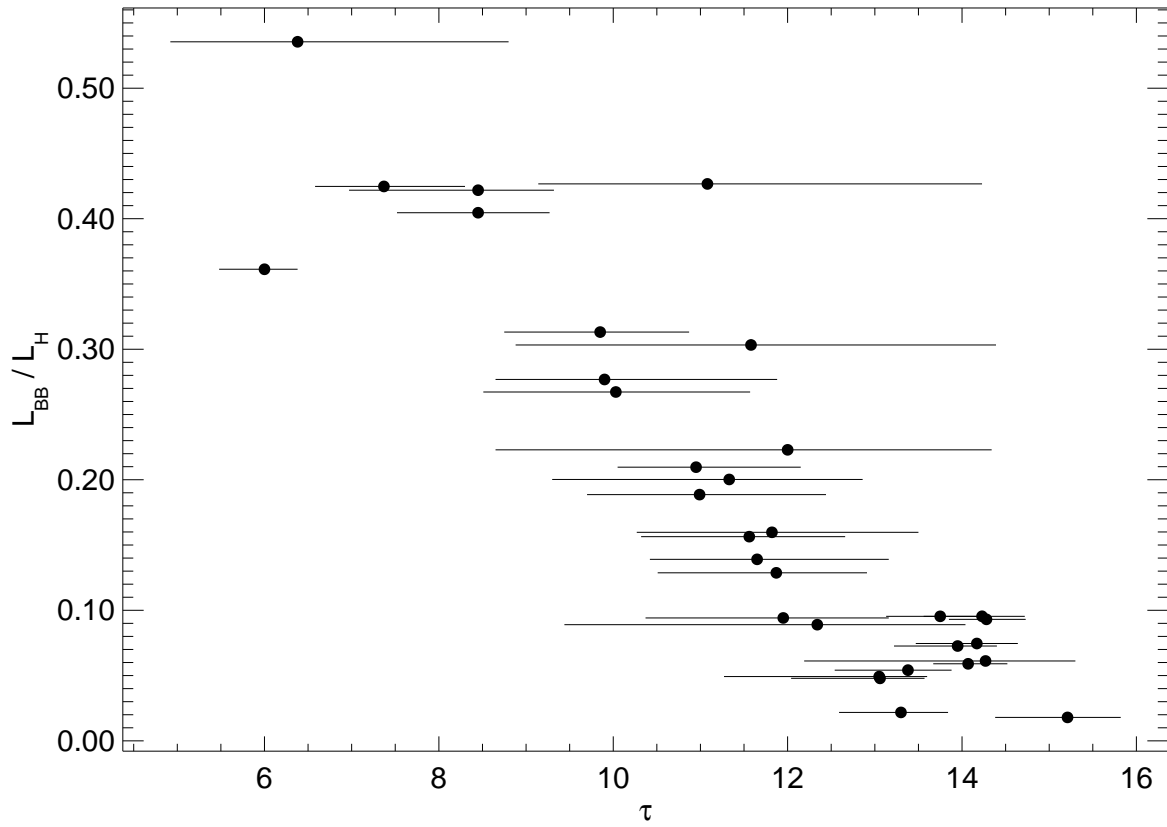


Fig. 11.—